2017-01-01

A Quantitative Analysis of the Fretted Terrain Valleys, Arabia Terra, Mars

Kelsey Anne Mason
University of Texas at El Paso, kmaso270@gmail.com

A QUANTITATIVE ANALYSIS OF THE FRETTED TERRAIN VALLEYS, ARABIA TERRA, MARS

KELSEY ANNE MASON

Master's Program in Geological Sciences

APPROVED:

José M. Hurtado Jr., Ph.D., Chair

Terry Pavlis, Ph.D.

Patrick Whelley, Ph.D.

Charles Ambler, Ph.D.

Dean of the Graduate School

Dedication

I would like to dedicate this thesis to my mom, Jacquelyn Casale as well as my aunt, Kimberly Mason. Thank you both for always inspiring me to make my life an adventure and follow my dreams. I love you both to Mars and back!

A QUANTITATIVE ANALYSIS OF THE FRETTED TERRAIN VALLEYS, ARABIA TERRA, MARS

by

KELSEY ANNE MASON, B.S.

THESIS

Presented to the Faculty of the Graduate School of

The University of Texas at El Paso

in Partial Fulfillment

of the Requirements

for the Degree of

MASTER OF SCIENCE

Department of Geological Sciences

THE UNIVERSITY OF TEXAS AT EL PASO

December 2017

Acknowledgements

There are many individuals I would like to thank for helping me get to where I am today. First, I would like to thank my friends, especially John Olgin, Valeria Martinez, and Amanda Labrado. Thank you for not letting me give up and always reminding me I am smarter than I realize. Thank you to Dr. Patrick Whelley, Dr. Kelsey Young, Dr. Jacob Bleacher, and Dr. Jacob Richardson from NASA Goddard Space Flight Center for always making me feel like I will be successful in my career. Lastly, thank you to my advisor, Dr. José Hurtado for helping me to complete my thesis and motivating me to do the best that I can do always.

Abstract

Fretted terrain describes regions on Mars with low-lying, flat valleys separated by steep cliffs that often form polygonal-shaped mesas. The fretted terrain valleys have a morphology distinct from other valleys found on Mars, and their unknown origin may hold insights into critical questions about Mars' tectonic, magmatic, and hydrologic history. Current hypothesis for the formation of the fretted terrain include fracturing as well as hydrological flow processes such as fluvial or glacial erosion. The region for this study is located in eastern Arabia Terra and is the type-location for fretted terrain. By qualitatively and quantitatively documenting the planform, or map-view, valley geometries and orientations throughout the fretted terrain, this study better constrains the origin of the valleys. Valleys were mapped using automated routines in ArcGIS including the D8 flow direction algorithm. Valleys were then grouped geographically into basins and also by Strahler order. The valleys were then segmented every 50 km and the azimuth of each segment was calculated. The resulting valley azimuths were analyzed using rose diagrams to quantitatively describe the planform geometries of the valleys. Qualitatively, the majority of basins were found to have rectangular valley geometries. The downslope direction was calculated for each basin, and it was compared to the corresponding valley azimuths. The basins with rectangular valley geometries had valleys with an azimuth mode nearly parallel to the downslope direction and another azimuth mode perpendicular to the downslope direction. The valley azimuth mode parallel to the downslope direction is attributed to hydrological flow processes while the mode perpendicular to the downslope direction is attributed to fracturing related to the formation or existence of the Mars global dichotomy boundary.

Table of Contents

List of Tables

List of Figures

1. Introduction

The fretted terrain on Mars is characterized by low-lying valleys separated by polygonal mesas with steep cliffs (Sharp, 1957) that formed during the Middle Noachian to Early Hesperian (McGill, 2000). Fretted terrain valleys display features distinct from other valleys on Mars, and, therefore, they are hypothesized to have a unique origin (Sharp, 1957). The northeastern ~2.6 x 10^6 km^2 of Arabia Terra (Figure 1) is the type location for fretted terrain on Mars (Sharp, 1957). The fretted terrain within Arabia Terra is the focus of this study due to its unexplained origin and its proximity to several geological features of interest that date back to early Mars history. These features include:

1. The "global dichotomy boundary", an approximately 3.9 Ga escarpment that separates the southern hemisphere highlands from the northern hemisphere lowlands (Werner, 2009). There are several hypotheses for the origin of the dichotomy boundary including: a giant impact (Frey and Shultz, 1998); mantle convection (Roberts and Zhong, 2006); and lithospheric flexure (Watters, 2003).

2. Recently identified evidence for Late Noachian explosive super eruptions in northwestern Arabia Terra (Michalski and Bleacher, 2013). The processes behind the origin of these suggested volcanoes are still unclear.

3. The Late Noachian to Early Hesperian friable material (Hynek et al., 2003) composing the fretted terrain. The friable material's composition has been difficult to determine because spectral measurements are hampered by pervasive dust cover in the Arabia Terra region (Kerber et al., 2012). The fine-

grained deposit has previously been suggested to be an explosive volcanic deposit due to the thickness, layering, zonal indurations, and draped morphology it exhibits (Moore, 1990). Others, however, have suggested it has an aeolian (Grant and Schultz, 1990) or paleopolar (Schultz and Lutz, 1988) origin.

Because its origin is uncertain, and because of its potentially critical relationship to volcanotectonic, climatic, and hydrologic processes during early Mars history, further study of the origin of the fretted terrain is warranted.

The processes hypothesized to have had a role in the formation of the fretted terrain range from fracturing (Sharp, 1973; Irwin et al., 2004; this study) possibly related to volcanism or regional tectonics, to hydrological flow processes, i.e. surface water erosion due to glaciers and/or rivers (Breed et al., 1982; Carr, 2001; Fairén et al., 2011). In this study, I analyze the extent to which valleys within the northeastern Arabia Terra fretted terrain morphologically resemble an ancient fracture system or an ancient drainage network. Valleys were mapped throughout the fretted terrain using automated algorithms and the map-view, or planform, geometries of the valleys were analyzed. In addition, the relationships between the valleys and the basin-scale topography (downslope direction and slope) were analyzed. These data are then used to provide insight into the origin of the fretted terrain and its implications for the hydrologic, climatic, and tectonomagmatic history of ancient Mars.

2. Background

2.1 Ancient Hydrologic, Climatic, and Tectonomagmatic History of Mars

During the Middle Noachian to Early Hesperian, the time when the fretted terrain is thought to have formed (McGill, 2000), Mars was likely much wetter than it is today (Poulet et al., 2005). In fact, most of the valley networks found on Mars, including those in the Arabia Terra fretted terrain, formed during this time (Carr and Chuang, 1997). Valley networks on Mars are described as a "complex system of hierarchically coalescing channels" (Stepinski and Collier, 2004), and they resemble terrestrial fluvial systems in that they are downslope-oriented (Stepinski and Collier, 2004) and have similar planform morphologies (Carr, 1995). Thus, the martian valley networks are thought to have formed by surface runoff, similar to fluvial networks on Earth (Stepinski and Collier, 2004).

There are, however, some important differences between terrestrial fluvial networks and martian valley networks. For example, most martian valley networks have U-shaped and rectangular-shaped cross sections (Carr, 1995) and have much smaller drainage densities (Stepinski and Collier, 2004). These dissimilarities have motivated other hypotheses for valley network formation on Mars including groundwater sapping (Carr, 1995), water-lubricated mass wasting (Carr, 1995), glaciers (Forget et al., 2006), and ground water flow (Malin and Carr, 1999). Nevertheless, valley networks are still one of the key pieces of evidence to support the hypothesis of a once warm and wet Mars (Stepinski and Collier, 2004). However, the warm and wet Mars hypothesis has been disputed based on the lack of an adequate warming mechanism (Tian et al., 2009).

The most recent database of martian valley networks was produced by Hynek et al. (2010) using Thermal Emissions Imaging System (THEMIS) daytime IR data (100 m/pixel) combined with Mars Orbiter Laser Altimeter (MOLA) data (463 m/pixel). Hynek et al. (2010) identified valley networks as those that branch, or have a tree-like planform morphology, with the smaller valleys upslope connecting to the larger valleys downslope, similar to fluvial valley networks on Earth. It is important to note that the criteria for identifying valleys used by Hynek et al. (2010) is different than that used in this study (see Section 3 for details). Therefore, the valley database in this study will include some valleys not mapped by Hynek et al. (2010) and also exclude some valleys that were mapped by Hynek et al. (2010). Due to this difference in definition, the valleys in this study will be referred to as "valley systems" as opposed to "valley networks".

Along with fluvial activity potentially having occurred within the Arabia Terra fretted terrain region during the Noachian, there is also substantial evidence for glaciation having occurred throughout the region during the Late Amazonian (Dickson et al., 2008). Evidence includes lineated valley fill and lobate debris aprons that appear to stem from alcoves and follow a downslope trajectory (Dickson et al., 2008). It, therefore, is possible that flowing ice may have also had a role in the formation of the valley networks.

During the time of the Arabia Terra fretted terrain formation, Mars was more volcanically and tectonically active than it is today (Werner, 2009). Nearby volcanic constructs thought to have been active during the time of fretted terrain formation include plains-style caldera complexes to the west (i.e. Eden Patera (33.6°N, 348.9°E); Michalski and Bleacher, 2013) and the Syrtis Major region (Hiesinger and Head, 2004) to the south (Figure 1). Michalski and Bleacher (2013) suggest the plains-style caldera complexes formed due to the already thin Arabia Terra crust and an extensional event that occurred during the Late Noachian to Early Hesperian. Syrtis Major is

thought to have formed during the Early Hesperian (Hiesinger and Head, 2004), and crustal thickness data suggests it does not have an origin related to the impact that formed the nearby Isidis Basin (Hiesinger and Head, 2004). Therefore, tectonic events such as extension may have played a role in the development of Syrtis Major. Some hypotheses for the origin of the dichotomy boundary, on which the fretted terrain is imprinted, also involve tectonic processes. These hypotheses include lithospheric flexure caused by loading of the northern lowlands (Watters, 2003) and mantle convection (Roberts and Zhong, 2006).

2.2 Hypotheses for the Formation of the Fretted Terrain

The fretted terrain was first described by Sharp (1973) who claimed the fretted terrain originated by escarpment recession, based on the pervasiveness of talus slopes along the margins of the mesas (Sharp, 1973). Since then, other studies have suggested that the valleys were cut by glaciers (Lucchitta, 1984; Fairén et al., 2011) or were strongly influenced by other erosional processes such as piping (Lucchitta, 1984), mass wasting (Carr, 1995), groundwater seepage (Carr, 1995), and/or fluvial erosion (Breed et al., 1982; Carr, 2001). There is substantial evidence for hydrological flow processes having occurred in this region, such as the presence of flow lineations (Head et al., 2006), debris aprons (Squyres, 1978; Head et al., 2006), and fluvial-like valley networks (Carr, 1995; Hynek et al., 2012). Apparently young (Amazonian) debris flow deposits also indicate that geomorphic processes within the Arabia Terra fretted terrain have been active relatively recently (Sharp, 1973). As such, it is likely that fluvial and/or glacial processes were important in the subsequent (and relatively recent) modification, of the fretted terrain valley systems. Yet, it is still unclear how much of an influence these hydrological flow processes had on the original formation of the fretted terrain valleys, if at all.

Previous studies have suggested the origin of the fretted terrain involved fracturing, based on the irregular pattern of the valleys (Irwin et al., 2004), or, at minimum, that some form of structural control was important for valley formation by erosion (McGill, 2000). This study also provides evidence in support of a fracture origin.

2.3 Using Valley Planform Morphology to Characterize Lithology

This study assumes that hydrological flow processes, here referring to fluvial, glacial, or groundwater flow, dominantly occur in the downslope direction unless otherwise influenced by lithologic or structural heterogeneities. For example, structures (folds, fractures, faults, etc.) formed by tectonic processes have been proven to influence drainage networks on Earth (Caputo et al., 1993). Because of this relationship between geologic structures and drainage networks, the planform geometry of valley systems can reveal information about lithologic and structural heterogeneities in the substrate into which the valleys are carved (Hugget, 2007). For instance, on Earth, rectangular geometries imply fluvial systems controlled by orthogonal fracture systems, while trellis drainage geometries can indicate folds (Hugget, 2007). Dendritic drainage patterns indicate fluvial systems formed in a homogeneous substrate (Hugget, 2007), while parallel drainage patterns may indicate a homogeneous substrate if the regional slope is steep (>1.3°) or a unimodal fracture system in the substrate if the regional slope is shallow (<1.3°) (Mangold et al., 2004; Hugget, 2007).

3. Methods

To determine the mechanism(s) involved in the formation of the fretted terrain valleys, I interrogated Mars topographic data using ArcGIS version 10.4.1 (Figure 2). This study assumes that the morphology of valley systems formed by fluvial processes are a function of the substrate lithology into which they are cut (Mejía and Neimann, 2008). Another important assumption is that hydrological flow processes will carve features following the regional downslope direction if no heterogeneities exist within the substrate such as fracturing. Most previous studies on the origin of the fretted terrain have focused on qualitative geomorphologic descriptions. Our contribution includes a detailed quantitative analysis of the valleys.

3.1 Data

This study utilizes topographic data from the Mars Orbiter Laser Altimeter (MOLA; Zuber et al. 1992). MOLA started mapping Mars in September of 1999 (Smith et al., 2001) and continued until it was decommissioned in 2001. MOLA mapped the topography of the surface of Mars by measuring time-of-flight and pulse-spread of 10 Hz laser pulses that were emitted by the instrument and reflected back to the instrument by the martian surface (Som et al., 2008). The primary goal of MOLA was to generate a global topographic map of Mars to aid in geophysical, geologic, and atmospheric studies (Smith et al., 2001).

For this study, the highest-resolution MOLA gridded topography dataset was used (Smith et al., 2001). The 128 pixel-per-degree (463.0836 m/pixel) MOLA Digital Elevation Model (DEM) was obtained from the NASA Planetary Data System (PDS) through the USGS Astrogeology Science Center (Smith et al., 2003). A DEM is an evenly spaced regular grid wherein each pixel

represents an elevation value. In the case of the MOLA DEM, the gridded elevation values have been interpolated from the laser range postings using a minimum-curvature-under-tension (MCUT) scheme as described by Som et al. (2008). The elevation values in the MOLA DEM represent elevation above the aeroid, determined from Mars gravity field solution GMM-2B (Lemoine et al., 2001). The total elevation uncertainty in this DEM is ±1.8 m (Lemoine et al., 2001).

3.2 Study Area

Between the southern highlands and the northern lowlands of Mars lies the fretted terrain. The fretted terrain covers 3% of the martian surface and contains irregularly oriented enigmatic erosive features, which produce steep escarpments of uniform height (1 to 2 km) and smooth low-lying valleys (Sharp, 1973). The type location for fretted terrain is in northeastern Arabia Terra between 30° and 40° N and 10° and 80°E, and is the area of focus for this study (Sharp, 1973; Figure 1). Lithologically, the fretted terrain in this region is primarily composed of discontinuous, friable, Late Noachian to Early Hesperian material (Hynek et al., 2003; Fassett and Head, 2007; Kerber et al., 2012). As described previously, this material has been interpreted to be an explosive volcanic deposit (Moore, 1990), an aeolian deposit (Grant and Schultz, 1990), or a paleopolar deposit (Schultz and Lutz, 1988). The characteristic fretted texture is thought to have originated during the Middle Noachian to Early Hesperian (McGill, 2000), but did not form all at once (Sharp, 1973). Tectonic features of interest in the study region include extensional grabens documented on the most recent global geologic map of Mars by Tanaka et al. (2014; Figure 1b).

3.3 Delineating the Basins and Valley Network Using Automated Algorithms

Data preprocessing involved using ArcGIS to extract from the MOLA DEM a map of drainage basins and valley systems in Arabia Terra. Previously, mapping of martian valley networks has been done primarily by hand using THEMIS daytime IR data combined with MOLA data (Hynek et al., 2010) rather than using automated algorithms and DEM data as is done in this study. This is, in part, due to THEMIS data having better spatial resolution than the globally available MOLA DEM (100 m/pixel vs. 463 m/pixel). In addition, the MOLA DEM was generated by interpolation of point elevation values, and it therefore contains inherent elevation errors. The elevation errors cause some valleys to go unidentified when using automated algorithms (Hynek et al., 2010). The distribution of the elevation error is a product of how the point elevation data were originally collected by the MOLA instrument (Som et al., 2008). Although the resolution of the MOLA DEM is poorer than that of other globally available data, the methods in this study rely on the use of a DEM, and the features of interest (i.e. the valleys) are much larger than the resolution of the DEM.

This study followed the methodology of Stepinski and Collier (2004) to generate a map of valley systems from DEM data. The workflow is shown schematically in Figure 2. First, the MOLA DEM was digitally filled in order to remove data artifacts and internally drained basins such as impact craters, which in this study area were 400 km in diameter or less (Figure 3). Drainage basins and valley systems were then mapped from the filled MOLA DEM using the D8 flow direction algorithm (Tarboton, 1997) implemented in the Flow Direction tool in ArcGIS (Figure 4). The D8 algorithm has been applied previously to topographic data of Mars (Stepinski and Collier, 2004) and Earth (Persendt and Gomez, 2016) for objectively mapping valley networks and associated drainage patterns. Using the Flow Direction tool implementation of the D8

algorithm, a flow direction raster was generated from the filled DEM wherein each pixel represents the direction in which surface water would flow (i.e. towards the pixel in the eight-neighborhood with the lowest elevation). From the flow direction raster, drainage basins were then generated using the Drainage Basin tool in ArcGIS. This tool locates points in the flow direction raster where the water would "flow out" of the raster (i.e. "pour points") and defines the drainage basins as the areas that contribute to each of those points. Subsequently, the Flow Accumulation algorithm in ArcGIS was used to generate a flow accumulation raster from the flow direction raster wherein each pixel value is the total number of pixels that "flow" through that location (Stepinski and Collier, 2004).

The higher the flow accumulation values, the more likely water would accumulate in that area. Therefore, a flow accumulation threshold value must be chosen to distinguish likely valley locations. A threshold value of 11,000 pixels was chosen based on trial-and-error in order to meet two criteria: (1) the threshold must be small enough to reveal the geometry of the networks; and (2) the threshold must be large enough so that DEM generation artifacts are not introduced (Figure 5). Unlike in the Stepinski and Collier (2004) study, the choice of an optimal threshold value is less crucial for the purposes of this study because drainage density is not being calculated. Instead, this study is interested in the geometry of the valley systems, which is not strongly dependent on an accurate drainage density.

After the threshold was applied to the flow accumulation raster, the ArcGIS Stream Order tool was used to assign Strahler order values (Strahler, 1973) to each valley segment (Figure 6). Higher Strahler order valleys are typically wider and have more discharge and drainage area than their lower order counterparts (Strahler, 1957). Therefore, if the high Strahler order valleys were formed by hydrological flow processes, their orientations are expected to closely mimic the

regional downslope direction. The Raster to Polyline tool was then used to generate a valley vector map. In the resulting valley maps, valleys were removed manually that appeared to be artifacts in that they did not correspond to topography and follow the DEM grid. The polyline valleys were then segmented into 50-km long reaches using the ArcGIS Construct Points and Split Line at Point tools. The 50-km length was chosen based on the apparent scale of major changes in the orientation of the valleys, with care taken to not make the segment length so small as to include DEM generation artifacts which are apparent at scales < 50 km.

3.4 Calculating Valley Azimuths

A total of 1,748 valley segments were generated and saved as a polyline shapefile in ArcGIS. The azimuth of each valley segment was calculated using codes written in Python and VBScript to interface with the Field Calculator in ArcGIS (Figure 7; Appendix A). First, the coordinates of the starting (x_0, y_0) and ending (x_1, y_1) points for each segment were found using the Calculate Geometry option in the attribute table for the valley shapefile in ArcGIS. These data were input to the code described in Appendix A. The code calculates the distance between the starting and ending points (Δx, Δy) of each valley segment. The azimuth (θ) of the reach (in radians) is then computed using:

$$\theta = \tan^{-1}\left(\frac{y_0 - y_1}{x_0 - x_1}\right) \qquad (1).$$

The azimuth values were subsequently converted to degrees, and 180° was added to values less than zero to produce an azimuth range between 000 and 180. It should be noted that the resulting azimuth values are rotated and reflected with respect to conventional geographic coordinates such that north is equivalent to 090, east is equivalent to 000, west is equivalent to 180, and south is

equivalent to 270. This azimuth scheme was retained for computational purposes in the workflow. However, for presentation purposes, the azimuth data and results shown here in all tables and figures have been corrected to conventional coordinates such that north is 000, east is 090, west is 270, and south is 180.

3.5 Generating Rose Diagrams

Rose diagrams are a method for displaying circular azimuth data in a manner similar to a histogram. In this study, rose diagrams were plotted for valley azimuth values. A rose diagram was generated for each of the basins in order to document spatial patterns between regions within the study area. Rose diagrams were generated that include all of the valleys in each basin, and rose diagrams were also generated for valleys grouped by Strahler order in each basin.

To construct the rose diagrams, valley azimuth values were first classified into 18 10° azimuth bins using if-then statements written in Python to interface with the ArcGIS Field Calculator (Appendix B). The length of each valley segment was found using the Calculate Geometry option in the attribute table for the valley shapefile in ArcGIS. Total lengths for each of the valley classes were calculated in Microsoft Excel. The percentage of valley lengths that fell into each azimuth bin were then calculated for each basin (Appendix C). Those values were input into the MATLAB code shown in Appendix D, which generates the rose diagrams. Each petal in the rose diagrams corresponds to an azimuth interval of 10°, while the lengths of the petals correspond to the percent of valley lengths that fall into each azimuth bin. It should be noted that although the valley azimuth measurements fall between 000 and 180, the values were reflected to generate a complete rose diagram with values between 000 and 360.

3.6 Determining Azimuth Modes

The resulting rose diagrams show multi-modal distributions of azimuths. In order to determine which azimuth modes should be considered significant, this study used the approach of Richardson et al. (2013). The mean and standard deviation of rose diagram bin values were calculated, and bin values greater than the mean plus one standard deviation ($\mu+1\sigma$) were considered statistically significant modes. The "$\mu+1\sigma$" threshold value is indicated on the rose diagrams by a dashed circle.

3.7 Classifying Planform Valley Geometries

The planform geometries (i.e. dendritic, rectangular, parallel, etc.; Figure 8) of the valley systems were assessed qualitatively based on apparent valley intersection angles as indicated in the vector maps and quantitatively based on the valley orientations as indicated in the rose diagrams. Parallel drainage networks have very acute angles of intersection and tend to have subparallel valley orientations, whereas rectangular networks have orthogonal valley orientations (Mejía and Neimann, 2008). Dendritic patterns have a range of acute angles of intersection (Mejía and Neimann, 2008).

In order to classify the valley morphologies quantitatively, the valley azimuth modes for each basin were analyzed. Basins with two statistically significant modes 60°-90° apart were considered rectangular, basins with mode(s) ≤30° apart where taken as parallel, and basins with mode(s) ≤60° and >30° apart were taken as dendritic (Figure 8). In the cases where the planform geometry of the valleys was classified as parallel, the regional slope was also taken into

consideration when categorizing the origin of the valleys. For example, parallel valleys in a region with a slope <1.3° were considered to be caused by a unimodal fracture system (Mangold et al., 2004).

3.8 Calculating the Downslope Direction and Slope

The downslope direction for each drainage basin was found by randomly selecting 1% of the pixels from the corresponding portion of the MOLA DEM and employing the Trend tool in ArcGIS to fit a planar surface to the selected elevation values using a least-squares regression (Figure 9). Then, the slope and aspect of the best-fit plane was determined using the Slope and Aspect tools in ArcGIS. In this study, the aspect (horizontal projection of the orientation of the surface normal) of the best-fit plane is taken to be the downslope direction. The downslope direction represents the expected preferred orientation for valley systems erosively carved by hydrological flow processes. Increasing the number of pixels selected for use in the least-squares regression did not drastically change the resulting orientation of the best-fit plane and the orientation of the downslope direction.

The azimuths of valleys as categorized by Strahler order, as well as the azimuths of all valleys within each basin were compared to the downslope direction. Our assumption is that the more similar the valley azimuths are to the downslope direction, the more likely an origin via hydrological flow processes, whereas the further the values are from each other, the more likely the orientations of the valleys are influenced by other factors such as fracturing. Because hydrological flow processes are expected to operate nearly parallel to the downslope direction and fracturing may occur at arbitrary angles with respect to downslope direction, valleys with modes

30° to 90° away from the downslope direction are taken to be consistent with fracturing, while valleys with a more acute relationship (i.e. <30°) to the downslope direction are taken to be consistent with either fracturing or hydrological flow processes.

3.9 Valley Sinuosity Index

Sinuosity describes how curved or straight a valley is. On Earth, most valleys with a fluvial origin uninfluenced by fracturing have sinuosity values close to 2 (Mueller, 1986), while valleys generated or influenced by fracturing may have a low sinuosity close to 1. Valleys generated by fluvial processes may have sinuosity values approaching 1 if the terrain is steep, however, in the fretted terrain region, the terrain has a very gradual slope (~0.23°). To calculate sinuosity index values (S), the total length (l) of each valley segment was divided by the length of a straight line joining the start of the segment (x_0, y_0) to the end of the segment (x_1, y_1) (Figure 10):

$$S = \frac{l}{\sqrt{(y_0 - y_1)^2 + (x_0 - x_1)^2}} \qquad (2).$$

Index values close to 1 indicate a straight valley, suggesting a possible fracture origin, while values greater than 1 indicate more sinuous values with a more likely fluvial origin. Sinuosity index values were calculated for all valleys, as well as just the valleys with statistically significant azimuth modes in order to better constrain their potential origin.

4. Results

4.1 Planform Geometries

In qualitative terms, basins 1-3 (9% of the total study area) display a parallel geometry while basins 4-9 and 11 (89% of the total study area) display a rectangular geometry (Appendix E, Figures E1-E11). Quantitatively, if only the valleys with statistically significant azimuths are considered, basins 1-3 are classified as having a parallel geometry. Basins 5, 7, 8, and 11 (36% of the total study area) have two distinct modes 60°-90° apart, which categorizes them as rectangular (Table 1). Basin 10 (2% of the total study area) does not have enough recognizable tributaries to determine its geometry either quantitatively or qualitatively. Quantitatively determining the geometry of basins 4, 6, and 9 (53% of the total study area) is also difficult as the valley azimuth modes of these basins do not match the expected patterns as described previously in Section 3.7 (Figure 8).

4.2 Valley Azimuth Modes and the Downslope direction

The downslope direction and valley azimuth modes are shown graphically in Figures F1-F11 (Appendix F). Table 1 lists the slope and downslope direction values for each basin along with the corresponding root-mean-square error (RMSE) values for the best-fit plane used to calculate the slope and downslope direction. The RMSE values range from 97.6 m to 719.6 m. Smaller basins tend to have smaller RMSE values than the larger basins because the larger basins have more intra-basin relief and therefore the terrain deviates more from the best-fit plane.

Table 2 lists the azimuth values for the statistically significant modes for the valleys within each basin. Basins 1, 5, 7, 8, and 10 have valley azimuth modes that nearly parallel the downslope

direction (<30° difference), while basins 4-9 have modes that are nearly perpendicular to the downslope direction (60°-90° difference). Basins 2, 3, 6, 10, and 11 have modes with an acute relationship to the downslope direction (30°-60° difference).

The azimuth data for the valleys as categorized by basin and by Strahler order are shown in Table C2 (Appendix C). Valleys with Strahler order >2 are considered high Strahler order valleys. The high order valleys within basins 2, 4, 5, 7, 10, and 11 have azimuth modes that follow the downslope direction (<30° difference), while high order valleys within basins 1, 3, 4, 5, 6, 7, 8, 9, and 11 have azimuth modes >30° from the downslope direction (Appendix F). Valleys with an order of 1 or 2 are considered low Strahler order valleys. The low order valleys within basins 1, 2, 4, 5, 8, 9, and 11 have azimuth modes that follow the downslope direction, while low order valleys within all basins (1-11) have azimuth modes >30° from the downslope direction (Appendix F).

4.3 Sinuosity

Figure 11 shows a map of valleys color coded by their sinuosity. The average sinuosity values for basins 1-3 (1.13, 1.15, and 1.13) are higher than those for all of the other basins to the east, except for basin 11 (1.14). Valleys in basins 4-10 have average sinuosity values ranging from 1.09 to 1.12 (Table 1). Average sinuosity values for valleys corresponding to each statistically significant mode can be found in Table 2. The average sinuosity for valley modes that approximately follow the downslope direction is 1.13, while the average sinuosity for valleys with modes approximately perpendicular to downslope direction is 1.08. These results show that valleys

following the downslope direction are more sinuous than the valleys perpendicular to the downslope direction.

5. Discussion

5.1 Planform Geometries

The regional slope for basins 1-3 is low (<1.3°). This suggests that the parallel nature of the valleys in basins 1-3 is likely caused by fracturing (Mangold et al., 2004). The rectangular pattern observed throughout basins 4-11 may indicate a bimodal fracture system (Hugget, 2007). It is also possible that one of the two valley azimuth modes (the one that parallels the downslope direction) in basins 4-11 may be an expression of hydrological flow processes, while the perpendicular mode represents a single unimodal fracture system that may have formed at the time of valley formation. The sinuosity values support this possibility in that the sinuosity of the valleys parallel to the downslope direction is higher than that of the valleys perpendicular to the downslope direction. This suggests that the former have been influenced more by fluvial processes than have the latter. However, because the difference in average sinuosity (0.057) is less than the standard deviation of sinuosity values within individual modes (0.11 to 0.34), this does not preclude the valleys that follow the downslope direction from having a fracture origin. There is little to no evidence for dendritic patterns in any of the fretted terrain valleys, which suggests that fluvial processes may not have been the dominant formation mechanism for the fretted terrain valleys.

Discrepancies exist between planform geometries as determined qualitatively vs. those determined quantitatively. While some basins (i.e. basins 4, 6 and 9) were categorized as rectangular using the qualitative method, they were not categorized as rectangular using the quantitative method. This discrepancy may be due to the rectangular nature of these valley systems being evident at length scales smaller than 50 km, less than the length (50 km) at which the valleys were segmented prior to calculation of azimuths. It is also possible that the orientations of

the rectangular valleys in basins 4 and 6 are changing within the basins, similar to how the rectangular valley modes change between basins. Therefore the aggregate valleys have apparently random orientations, but if the valleys were subdivided within the basins a rectangular relationship may be more apparent. This is especially possible because basins 4 and 6 are the largest. It should also be noted that, unlike the other basins, basins 4 and 6 display several large (>100 km diameter) impact craters with ring fractures (Appendix E, Figures E4 and E6). It appears that, although the DEM was filled to remove internally draining basins, some valleys within basins 4 and 6 follow impact crater ring fractures. These ring fractures may partially account for the difficulty in quantitatively determining the planform geometries of basins 4 and 6.

The valleys in basin 9 have a significant azimuth mode that is perpendicular to the downslope direction, but they do not have a significant mode parallel to the downslope direction as do the valleys in basins 5, 7, 8, and 10. Therefore, even though the qualitative classification of the valleys in basin 9 is rectangular, based on the quantitative classification used in this study, the valleys in basin 9 would be considered parallel. However, there are nearly enough valleys in basin 9 with azimuths close to the downslope direction to consider them a significant mode (7.9% compared to the "$\mu+1\sigma$" threshold of 8.4%; Appendix F, Figure F9), which would change the quantitative classification to rectangular. The valleys following the downslope direction are not concentrated in one direction, rather they are dispersed around the downslope direction (±40°). Due to intra-basin relief, valleys caused by hydrological flow processes may have azimuths in varying directions around the regional downslope direction (Appendix F, Figure F9). Therefore, basin 9 may be an example of a location where there is fracturing perpendicular to the downslope direction that has created one set of valleys, but the valleys approximately parallel to the downslope direction are instead caused by hydrological flow processes.

5.2 Valley Azimuth Modes and the Downslope Direction

Valleys with azimuth modes that follow the downslope direction (i.e. basins 1, 2, 4, 5, 7, 10, and 11) may indicate an influence by hydrological flow processes in their formation. Basins with significant valley modes perpendicular to the downslope direction may be indicative of fracturing (i.e. basins 1, 2, 4, 5, 8, 9, and 11). As the downslope direction rotates from northwest to northeast across the study area, the valley azimuth modes maintain their perpendicular relationship to the downslope direction. The valleys at a high angle (60°-90°) to the downslope direction are considered to be fracture-controlled. In the study region, the downslope direction seems to be controlled by the dichotomy boundary as it is the primary topographic feature at the ≥500 km scale and is the main source of basin-scale relief. Therefore, the valleys that seem to be related to fracturing perpendicular to the downslope direction may owe their existence to the dichotomy boundary.

5.3 Basins 4-11

Basins 4, 5, 9, 10 and 11 contain low Strahler order valleys with azimuth modes that mimic the downslope direction. Assuming that low Strahler order valleys (i.e. small and locally pervasive) are more strongly influenced by intra-basin topographic relief rather than the basin-scale relief, low Strahler order valleys may be influenced by intra-basin-scale phenomena. Valleys at this scale (<100 km) could be strongly influenced by fracturing. Therefore, the low Strahler order valleys that follow the downslope direction may have been influenced by fracturing or hydrological flow processes.

Compared to low Strahler order valleys, the orientation of large, regionally pervasive, high Strahler order valleys would be affected the most by the downslope direction if the valleys were carved by hydrological flow processes. Therefore, cases where the high Strahler order valleys have azimuth modes that follow the downslope direction (i.e. basins 4, 5, 7, 10, and 11) suggest an influence by hydrological flow processes. In contrast, high Strahler order valleys with azimuth modes that are perpendicular to the downslope direction (i.e. basins 4-9 and 11) suggest an influence by fracturing.

5.4 Basins 1-3

The western part of the Arabia Terra fretted terrain (i.e. basins 1-3) has valleys with parallel planform valley geometries that are distinct from the other basins to the east. Basins 1-3 also have unimodal valley azimuths and higher sinuosity index values than their eastern counterparts. Although the valley modes in basins 1-3 nearly follow the downslope direction, which may indicate the valleys formed by hydrological flow processes, the valleys display, both qualitatively and quantitatively, a parallel morphology, suggesting they are fracture-controlled. The difference in valley morphology between basins 1-3 and basins 4-11 could be due to several factors: the smaller size of basins 1-3 compared to the other basins; a difference in lithology; spatial variations in ancient or modern climate; or a spatial change in the fracture forming process. Another possibility is that the dichotomy boundary is not as well defined in this part of the Arabia Terra fretted terrain as it farther to the east. Therefore, the downslope direction around basins 1-3 may not be strongly influenced by the dichotomy boundary. Considering this, it may be that fracturing related to the dichotomy boundary may still have generated the valleys in basins 1-3, but they need not be perpendicular to the downslope direction.

5.5 Limitations of the D8 Flow Direction Algorithm

Two factors must be taken into consideration when applying the D8 flow direction algorithm to a DEM to objectively map valley systems.

First, the algorithm will not identify all valleys. This may be because some valleys:

a. have too low of an elevation gradient; or

b. are isolated from the rest of the valleys; or

c. are located where interpolation error is present in the DEM data; or

d. are too small to identify at the resolution of the DEM.

However, the goal of this study was not to exhaustively map all of the valleys within the fretted terrain. Instead, the goals was to observe regional drainage patterns, a task we believe has been accomplished by analyzing the nearly complete subset of valleys delineated using the workflow described in Section 3.3.

Second, the valleys that the algorithm identified incorrectly also must be considered. The error associated with this was minimized by choosing a specific threshold (i.e. 11,000 pixels) in the flow accumulation raster when delineating valleys, as discussed in Section 3.3. This error was also minimized by manually removing valleys that appeared to be artifacts (Figure 5).

5.6 Hypotheses for the Origin of the Arabia Terra Fretted Terrain

Based on our findings, we suggest that fractures controlled the geometry and orientation of valleys within basins 4-11 and possibly also the valleys within basins 1-3. We propose three possible scenarios for the generation of the fractures in the Arabia Terra fretted terrain (Figure 12). Each of these scenarios accounts for the development of a unimodal fracture system within the fretted terrain parallel to the dichotomy boundary and perpendicular to the downslope direction. It is important to note, however, that these hypotheses do not preclude subsequent erosion by hydrological flow processes from having further contributed to the development of the valley systems in the fretted terrain.

One possible scenario is escarpment retreat, as previously suggested by Sharp (1957). In this scenario, fracturing may be related to the formation of an escarpment (i.e. the dichotomy boundary). Due to gravitational relaxation and continual undermining of the escarpment by water or ice, material will have the propensity to break off and generate fractures parallel to the escarpment and perpendicular to the downslope direction.

A second hypothesis for the formation of the fracturing is draping of an extensive friable deposit onto the pre-existing dichotomy boundary. This hypothesis would be consistent with the hypothesis that the Arabia Terra deposits are volcanic in origin (Kerber et al., 2012), possibly ash or ignimbrite. This volcaniclastic material would likely have been erupted from a volcanic center within the nearby plains-style caldera complexes to the west (Michalski and Bleacher, 2013). Fracturing of ignimbrite deposits draped across pre-existing escarpments is seen on Earth at Lascar Volcano in Chile, which produced a 20-m thick flow over a 30-m scarp (Whelley et al., 2011). At Lascar Volcano, this process produced a component of fracturing that is parallel to the escarpment in areas proximal to the scarp (<50 m), and a second component of fracturing with more random

orientations in areas further from the scarp (>50 m; Whelley et al., 2011). This study reveals that fretted terrain valleys in Arabia Terra have a parallel relationship to a prominent escarpment (the global dichotomy boundary), similar to the fractures within the Lascar volcanic deposits. Explosive volcanic eruptions on Earth have been shown to deposit ash fall 1,000's of km from their source (Newhall and Self, 1982) and ash flow deposits 100's of km from their source (Branney and Kokelaar, 2002). However, on Mars, it has been shown that ash flows could travel much farther (three to four times) because of lower gravity and atmospheric pressure (Wilson and Head, 1994). Material from the plains-style caldera complexes (Michalski and Bleacher, 2013) or a similar explosive volcanic system within or around northern Arabia Terra, may have been deposited throughout the fretted terrain (Kerber et al., 2013).

A third hypothesis is that the fracturing may be related to mantle convection processes active during the formation of the dichotomy boundary (Roberts and Zhong, 2006) around 3.9 Ga (Werner, 2009). Mantle convection may have generated extension in the crust adjacent to the dichotomy boundary, forming grabens oriented perpendicular to the extension direction (Davis et al., 1942). This is consistent with Michalski and Bleacher's (2013) idea that the crust was thinning along the dichotomy boundary during the Late Noachian to Early Hesperian.

It is important to note that the three hypotheses discussed here are not mutually exclusive. Also, these hypotheses do not account for the valleys with azimuth modes that are not perpendicular to the downslope direction. However, we may consider the valleys with a parallel or acute relationship to the downslope direction in basins 4-11 to have been caused by hydrological flow processes. This is because hydrological flow processes tend to form in the downslope direction. These valleys are also more sinuous overall, and there is evidence in this region for hydrological flow processes having occurred (Stepinski and Collier, 2004, Dickson et al., 2008).

The valleys within basins 1-3 appear distinct in many ways to the valleys within the other basins. However, due to their hypothesized fracture origin, and their close proximity to valleys in basins 4-11, they were likely influenced by similar processes. Most of the aforementioned hypotheses for the formation of valleys within basins 4-11 rely on the consistently perpendicular relationship between the fracturing and the downslope direction as a proxy for the dichotomy boundary. In order to use the downslope direction as a proxy for the dichotomy boundary, the dichotomy boundary must be the dominant topographic feature in the region. In the case of basins 1-3, the dichotomy boundary is not as dominant as in basins 4-11. Therefore, relating the downslope direction to the dichotomy boundary in this region is not as reliable. As such, although the valleys within basins 1-3 do not display the expected perpendicular relationship to the downslope direction, they may still owe their origin to phenomena similar to those that shaped basins 4-11.

6. Conclusions

Evidence presented here in the form of valley orientations and morphologies suggests that most of the valleys within the Arabia Terra fretted terrain originated as fractures that were subsequently accentuated and modified by hydrological flow processes such as glaciers, mass wasting, and/or fluvial activity. The valleys that are perpendicular to, and have azimuths that change systematically with the downslope direction, as well as valleys in basins 1-3, are those interpreted to be controlled by fracturing. Because the downslope direction in this region is controlled primarily by the dichotomy boundary, we suggest that the fracturing is related to the formation or existence of the dichotomy boundary. It is possible that the valleys that are parallel to the downslope direction are also related to fracturing, but a strong influence from, or formation by, hydrological flow processes is supported for these valleys by their higher sinuosity index values and their relationship to the downslope direction.

Future work should include use of high-resolution imagery such as that provided by the Mars Reconnaissance Orbiter (MRO) High Resolution Imaging Science Experiment (HiRISE; 30 to 60 cm per pixel; McEwen et al., 2007) to map the lithology of the fretted terrain region to determine if the units resemble that of an explosive volcanic deposit, as well as to gain a more detailed geomorphological description of the fretted terrain valleys to aid in resolving their origin.

References

Breed, C.S., McCauley, J.F., and Grolier, M.J., 1982, Relict Drainages, Conical Hills, and the Eolian Veneer in Southwest Egypt: Applications to Mars: *Journal of Geophysical Research*, v. 87, p. 9,929-9,950.

Caputo, C., Ciccacci, S., De Rita, D., Fredi, P., Palmieri, E.L., and Salvini, F., 1993, Drainage Pattern and Tectonics in Some Volcanic Areas of Latium (Italy): *Geologica Romana*, v. 29, p. 1-13.

Carr, M.H., 1992, Post Noachian erosion rates: Implications for Mars climate change: *Proceedings of the 24th Lunar and Planetary Science Conference*, v. 23, p. 205-206.

Carr M.H., 1995, The Martian drainage system and the origin of valley networks and fretted channels: *Journal of Geophysical Research*, v. 100, p. 7,479-7,507.

Carr, M.H. and Chuang, F.C., 1997, Martian drainage densities: *Journal of Geophysical. Research*, v. 102, p. 9,145-9,152.

Carr, M.H., 2001, Mars Global Surveyor observations of Martian fretted terrain, *Journal of Geophysical Research*, v. 106, p. 23,571-23,593.

Davis, G.H., Reynolds, and S.J., Kluth, C., 2011, *Structural geology of rocks and regions* (3rd Edition): John Wiley & Sons, Inc. (Hoboken, NJ), 864 p.

Dickson, J.L., Head, J.W., and Marchant, D.R., 2008, Late Amazonian glaciation at the dichotomy boundary on Mars: Evidence for glacial thickness maxima and multiple glacial phases: *Geology*, v. 36, p. 411-414.

Fairén, A.G., Davila, A.F., Gago-Duport, L., Haqq-Misra, J.D., Gil, C., Mckay, C.P., and Kasting, J.F, 2011, Cold glacial oceans would have inhibited phyllosilicate sedimentation on early Mars: *Nature Geoscience*, v. 4, p. 667-670.

Fassett, C.I. and Head, J.W., 2007, Layered mantling deposits in northeast Arabia Terra, Mars: Noachian-Hesperian sedimentation, erosion, and terrain inversion: *Journal of Geophysical Research*, v. 112, doi: 10.1029/2006JE002875.

Forget, F., Haberle, R.M., Montmessin, F., Levrard, B., and Head, J.W., 2006, Formation of Glaciers on Mars by Atmospheric Precipitation at High Obliquity: *Science*, v. 311, p. 368-371.

Frey, H. and Schultz, R.A., 1988, Large impact basins and the mega-impact origin for the crustal dichotomy on Mars: *Geophysical Research Letters*, v. 15, p. 229-232.

Frey H., Sakimoto and S.E., Roark, J., 1998, The MOLA topographic signature at the crustal dichotomy boundary zone on Mars: *Geophysical Research Letters*, v. 25, p. 4,409-4,412.

Grant, J.A. and Schultz, P.H., 1990, Gradational epochs on Mars: Evidence from west-northwest of Isidis basin and Electris: *Icarus*, v. 84, p. 166-195.

Head, J.W., Nahm, A.L., Marchant, and D.R., Neukum, G., 2006, Modification of the dichotomy boundary on Mars by Amazonian mid-latitude regional glaciation: *Geophysical Research Letters*, v. 33, doi: 10.1029/2005GL024360.

Hiesinger, H., Head, J. W., 2004, The Syrtis Major volcanic province, Mars: Mars Global Surveyor data: *Journal of Geophysical Research*, v. 109, doi: 10.1029/2003JE002143.

Hugget, R., 2007, *Fundamentals of Geomorphology* (2nd Edition): Routledge (New York), 458 p.

Hynek, B.M., Phillips, R.J., and Arvidson, R.E., 2003, Explosive volcanism in the Tharsis region: Global evidence in the Martian geologic record: *Journal of Geophysical Research*, v. 108, doi: 10.1029/2003JE002062.

Hynek, B.M., Beach, M., and Hoke, M.R.T., 2010, Updated global map of Martian valley networks and implications for climate and hydrologic processes: *Journal of Geophysical Research*, v. 115, doi: 10.1029/2009JE003548.

Irwin, R.P. and Watters, T.R, 2004, Sedimentary resurfacing and fretted terrain development along the crustal dichotomy boundary, Aeolis Mensae, Mars: *Journal of Geophysical Research*, v. 109, doi: 10.1029/2004JE002248.

Kerber, L., Head, J.W., Madeleine, J., Forget, F., and Wilson, L., 2012, The dispersal of pyroclasts from ancient explosive volcanoes on Mars: Implications for the friable layered deposits: *Icarus*, v. 219, p. 358-381.

Kerber, L., Michalski, J., Bleacher, J. & Forget, F, 2013, Ash sources in Arabia Terra? Implications for the Arabia Deposits: *Proceedings of the 44th Lunar and Planetary Science Conference*, Abstract 2290.

Lemoine, F.G., Smith, D.E., Rowlands, D.D., Zuber, M.T., Neumann, G.A., Chinn, D.S., and Pavlis, D.E., 2001, An improved solution of the gravity field of Mars (GMM-2B) from Mars Global Surveyor: *Journal of Geophysical Research*, v. 106, p. 23,359-23,376.

Lucchitta, B.K., 1984, Ice and Debris in the Fretted Terrain, Mars: *Journal of Geophysical Research*, v. 89, B409-B418.

Malin, M.C. and Carr, M.H., Groundwater formation of martian valleys, *Nature*, 397, p. 589-591.

Mangold, N., Quantin, C., Ansan, V., Delacourt, C., and Alleman, P., 2004, Evidence for Precipitation on Mars from Dendritic Valleys in the Marineris Area: *Science*, v. 305, p. 78-81.

McEwen, A.S., Eliason, E.M., Bergstrom, J.W., Bridges, N.T., Hansen, C.J., Delamere, W.A., Grant, J.A., Gulick, V.C., Herkenhoff, K.E., Kesthelyi, L., Kirk, R.L., Mellon, M.T., Squyres, S.W., Thomas, N., Weitz, C.M., 2007, Mars Reconnaissance Orbiter's High Resolution Imaging Science Experiment (HiRISE): *Journal of Geophysical Research*, v. 112, E05S02, doi: 10.1029/2005JE002605.

McGill, G.E., 2000, Crustal history of north central Arabia Terra, Mars: *Journal of Geophysical Research*, v.165, p. 6,945-6,959.

Mejía, A.I. and Niemann J.D, 2008, Identification and characterization of dendritic, parallel, pinnate, rectangular, and trellis networks based on deviations from planform self-similarity: *Journal of Geophysical Research*, v. 113, doi: 10.1029/2007JF000781.

Michalski, J.R. and Bleacher, J.E., 2013, Supervolcanoes within an ancient volcanic province in Arabia Terra, Mars: *Nature*, v. 502, p. 47-52.

Moore, J.M., 1990, Nature of the mantling deposit in the heavily cratered terrain of northeastern Arabia, Mars: *Journal of Geophysical Research*, v. 95, p. 14,279-14,289.

Persendt, F.C. and Gomez, C., 2016, Assessment of drainage network extractions in a low-relief area of the Cuvelai Basin (Namibia) from multiple sources: LiDAR, toographic maps, and digital aerial orthophotos: *Geomorphology*, v. 260, p. 32-50.

Poulet, F., Bibring, J.P., Mustard, J.F., Gendrin, A., Mangold, N., Langevin, Y., Arvidson, R.E., Gondet, B., and Gomez, C., 2005, Phyllosilicates on Mars and implications for early martian climate: *Nature*, v. 438, p. 623-627.

Roberts, J.H. and Zhong, S., 2006, Degree-1 convection in the Martian mantle and the origin of the hemispheric dichotomy: *Journal of Geophysical Research*, v. 111, doi: 10.1029/2005JE002668.

Richardson, J.A., Bleacher, J.E., and Glaze, L.S., 2013, The volcanic history of Syria Planum, Mars: *Journal of Volcanology and Geothermal Research*, v. 252, p. 1-13.

Schultz, P.H. and Lutz, A.B., 1988, Polar wandering of Mars: *Icarus*, v. 73, p. 91-141.

Sharp, R.P., 1973, Mars: Fretted and Chaotic Terrains: *Journal of Geophysical Research*, v. 78, p. 4,073-4,083.

Smith, D.E., Zuber, M.T., Frey, H.V., Garvin, J.B., Head, J.W., Muhleman, D.O., Pettengill, G.H., Phillips, R.J., Solomon, S.C., Zwally, H.J., Banerdt, W.B., Duxbury, T.C., Golombek, M.P., Lemoine, F.G., Neumann, G.A., Rowlands, D.D., Aharonson, O., Ford, P.G., Ivanov, A.B., Johnson, C.L., McGovern, P.J., Abshire, J.B., Afzal, R.S., and Sun, Xiaoli, 2001, Mars Orbiter Laser Altimeter: Experiment summary after the first year of global mapping of Mars: *Journal of Geophysical Research*, v. 106, p. 23,689-23,722.

Smith, D.E., M.T. Zuber, G.A. Neumann, E.A. Guinness, and S. Slavney, 2003, Mars Global Surveyor Laser Altimeter Mission Experiment Gridded Data Record: NASA Planetary Data System MGS-M-MOLA-5-MEGDR-L3-V1.0.

Som, S.M., Greenberg, H.M., and Montgomery, D.R., 2008, The Mars Orbiter Laster Altimeter dataset: Limitations and improvements: *Mars*, v. 4, p. 14-26.

Squyres, S.W., 1978, Martian Fretted Terrain: Flow of Erosional Debris: *Icarus*, v. 34, p. 600-613.

Stepinksi, T.F., and Collier, M.L., 2004, Extraction of Martian valley networks from digital topography: *Journal of Geophysical Research*, v. 109, doi: 10.1029/2004JE002269.

Strahler, A.N., 1957, Quantitative Analysis of Watershed Geomorphology: *Transactions, American Geophysical Union*, v. 38, no. 6, p. 913-920.

Tanaka, K.L., Skinner, J.A., Jr., Dohm, J.M., Irwin, R.P., III, Kolb, E.J., Fortezzo, C.M., Platz, T., Michael, G.G., and Hare, T.M., 2014, Geologic map of Mars: U.S. Geological Survey Scientific Investigations Map 3292, scale 1:20,000,000, https://dx.doi.org/10.3133/sim3292.

Tarboton, D.G., 1997, A new method for determination of flow directions and upslope areas in grid digital elevation models: *Water Resources Research*, v. 33, no. 2, p. 309-319.

Watters, T.R., 2003, Lithospheric flexure and the origin of the dichotomy boundary on Mars: *Geology*, v. 31, p. 271-274.

Werner, S.C., 2009, The global martian volcanic evolutionary history: *Icarus*, v. 201, p. 44-68.

Whelley, P.L., Jay, J., Calder, E.S., Pritchard, M.E., Cassidy, N.J., Alcaraz, S., and Pavez, A., 2011, Post-depositional fracturing and subsidence of pumice flow deposits: Lascar Volcano, Chile: *Bulletin of Volcanology*, v. 74, p. 511-531.

Yin, A., 2012, An episodic slab-rollback model for the origin of the Tharsis rise on Mars: Implications for initiation of local plate subduction and final unification of a kinematically linked global plate-tectonic network on Earth: *Lithosphere*, v. 4, p. 553-593.

Table 1: Basin Data

Basin Number	Qualitative Planform Morphology	Quantitative Planform Morphology	Downslope Direction (°)	RMSE (m)	Regional Slope (°)	Sinuosity	Cumulative Valley Length (km)	Basin Area (km^2)
1	Parallel	Parallel	334.9	173.7	0.22	1.13	2,735.8	151,882.2
2	Parallel	Parallel	338.6	123.7	0.18	1.15	1,111.1	68,145.1
3	Parallel	Parallel	344.2	97.6	0.10	1.13	777.7	47,850.8
4	Rectangular	Other	344.7	530.0	0.16	1.09	13,267.7	839,782.3
5	Rectangular	Rectangular	348.4	204.0	0.10	1.09	1,729.0	109,914.2
6	Rectangular	Other	344.7	719.6	0.24	1.09	7,083.1	492,766.8
7	Rectangular	Rectangular	15.0	642.6	0.30	1.11	4,052.2	291,631.5
8	Rectangular	Rectangular	23.4	545.9	0.23	1.12	7,684.4	465,501.8
9	Rectangular	Parallel	0.4	551.4	0.27	1.11	4,670.2	282,957.9
10	Other	Other	6.6	562.9	0.39	1.12	1,161.9	72,330.5
11	Rectangular	Rectangular	52.3	661.5	0.31	1.14	3,802.6	230,672.6

Table 2: Valley Data

Basin Number	Mode(s) (°)	Sinuosity	Degrees from Downslope Direction
1	130 to 150	1.14	14.9
2	110 to 130	1.16	38.6
2	90 to 100	1.13	63.6
3	100 to 120	1.18	54.2
4	90 to 100, 80 to 90	1.04	74.7
5	90 to 100	1.06	73.4
5	0 to 10	1.02	16.6
6	120 to 140	1.07	34.7
6	80 to 90	1.05	79.7
7	30 to 40	1.17	20.0
7	130 to 160	1.17	50.0
8	30 to 40	1.18	11.6
8	10 to 20	1.12	8.4
8	130 to 150	1.08	63.4
9	80 to 90	1.05	84.6
10	40 to 50	1.05	38.4
10	10 to 20	1.16	8.4
11	70 to 80	1.13	22.7
11	10 to 20	1.18	37.3

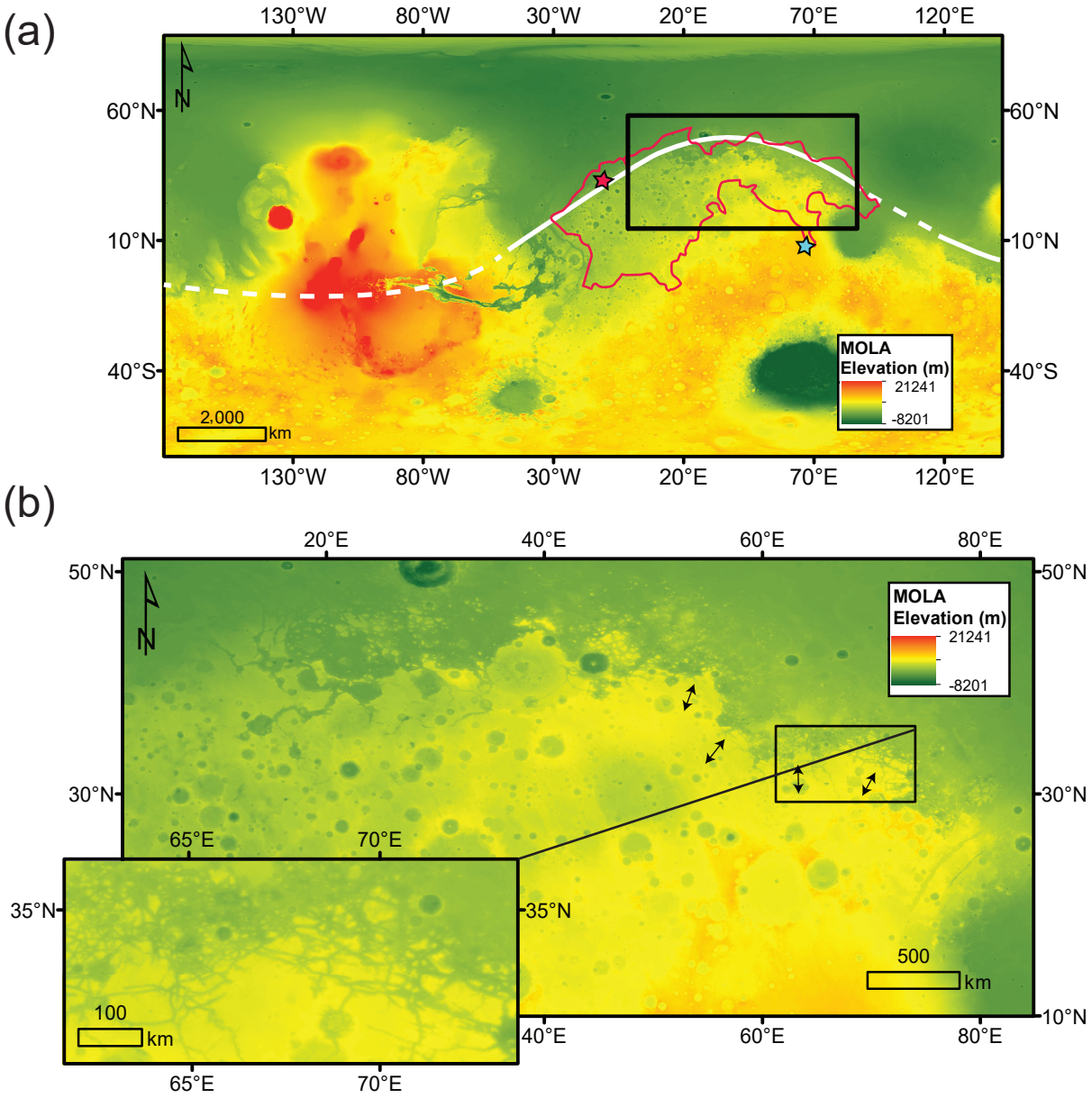

Figure 1: a) MOLA elevation map (MEGDR, Edition: 2003-03-21; Smith et al., 2001) of Mars. Black box outlines the area shown in (b). The white solid line represents the known global dichotomy boundary, while the white dashed line represents the inferred global dichotomy boundary (Yin, 2012). The red star with a black outline shows the location of Eden Patera, one of the plains-style caldera complexes suggested by Michalski and Bleacher (2013). The blue star with a black outline shows the location of Syrtis Major, another volcanic center (Hiesinger and Head, 2004). The solid red outlined polygon shows the location of the Arabia Terra friable deposits (Kerber et al., 2012). (b) MOLA elevation map (MEGDR, Edition: 2003-03-21; Smith et al., 2001) of the study area within the FT. Inset shows a more detailed view of the characteristic fretted texture. Black arrows symbolize tectonic extensional direction as suggested by Tanaka et al., 2014.

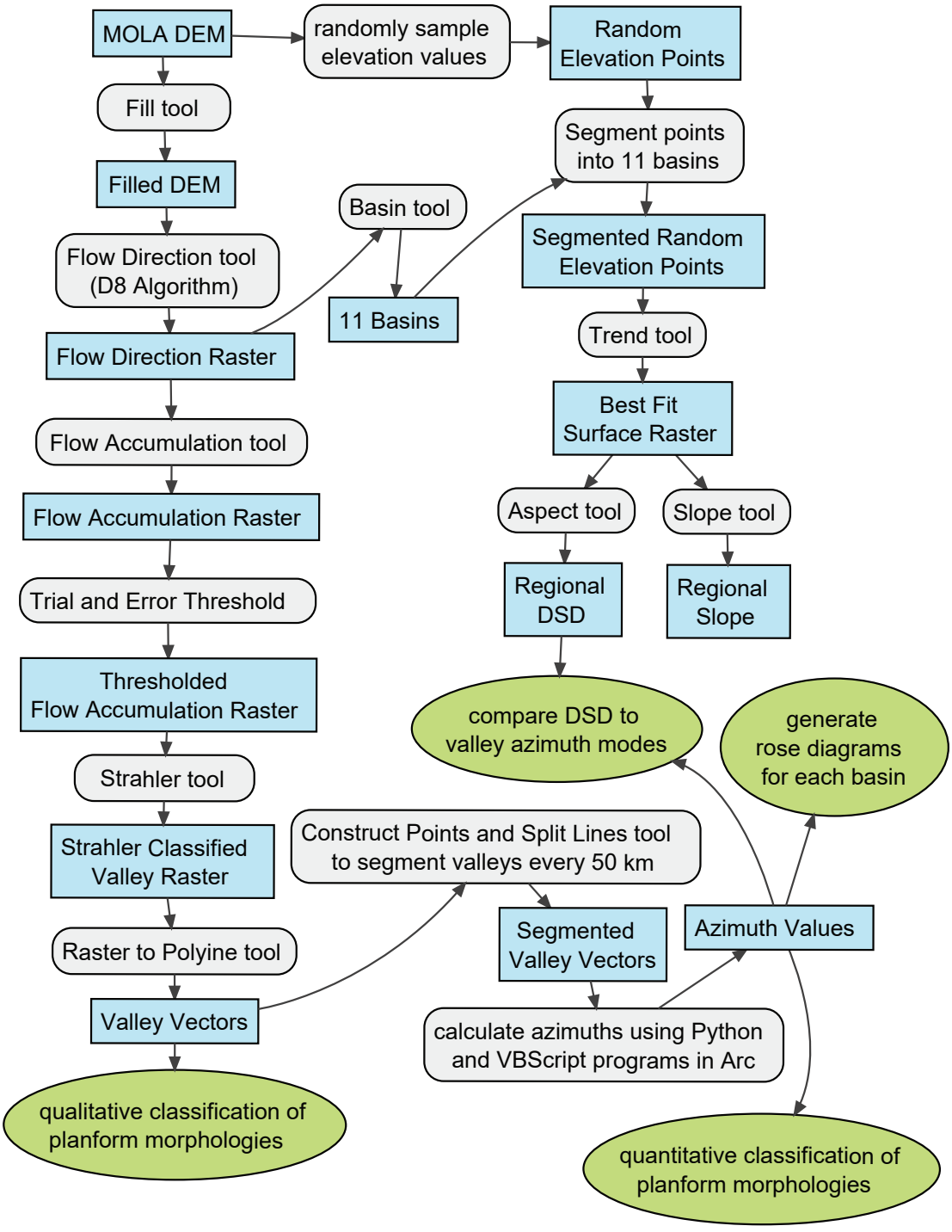

Figure 2: Flow chart showing generalized workflow for the generation of the Arabia Terra fretted terrain valley system and basins, the downslope direction values, regional slopes, and subsequent analyses. Gray rounded rectangles represent the operations performed in ArcMap, the blue rectangles represent the results of the operations and the green ovals represent analyses performed outside of ArcGIS.

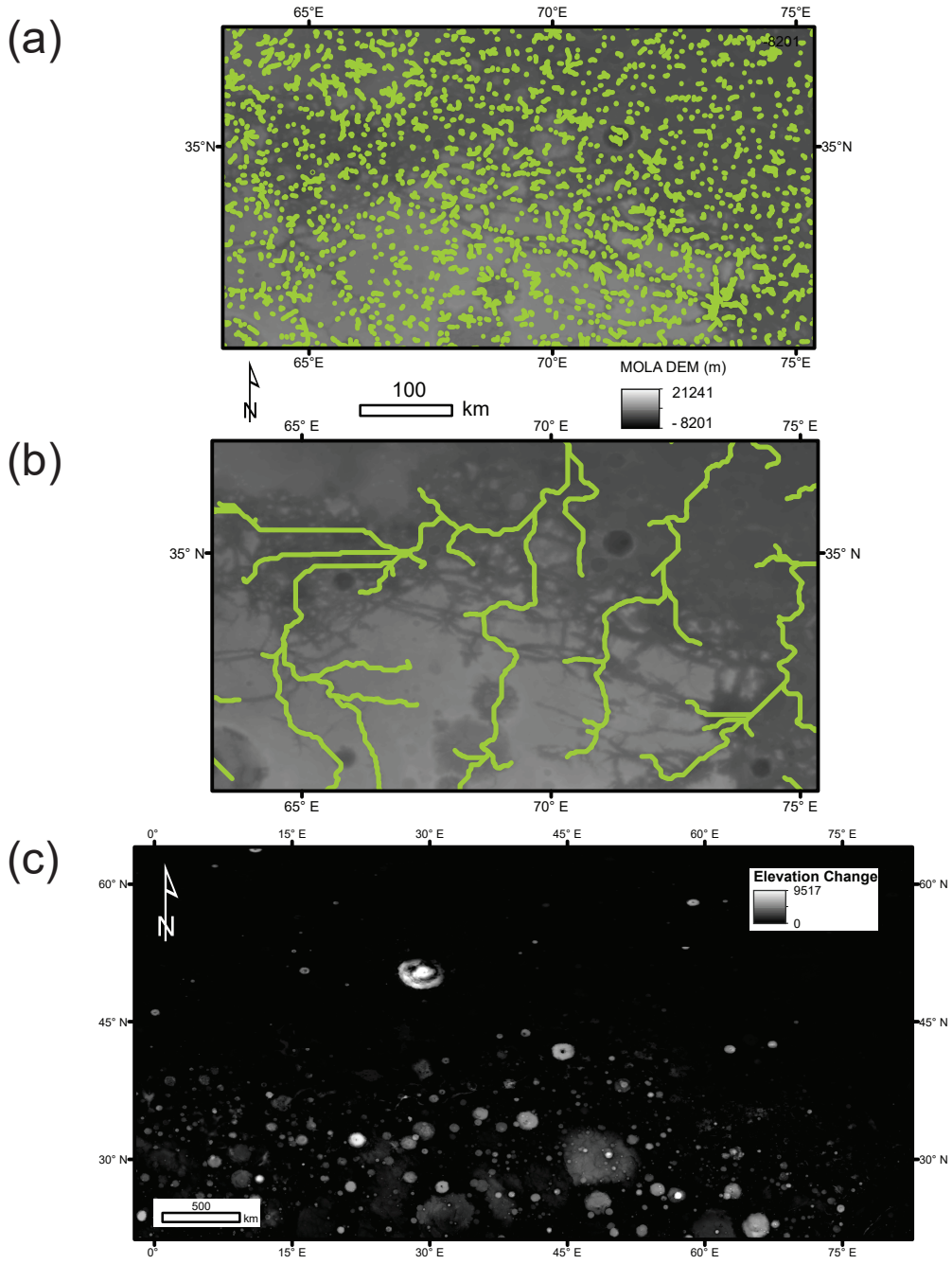

Figure 3: a) A portion of the MOLA DEM within the FT study area with the mapped valley system overlaid in green generated using a non-filled MOLA DEM. b) The same portion of the MOLA DEM as in a., however, overlaid in green are valleys generated using a filled MOLA DEM. c) Map of the entire study region showing elevation change (white equals highest elevation change) between the original and filled DEM. This figure is meant to emphasize the < 400 km internally draining impact crater basins that were filled in. This map was generated with the Raster Calculator tool in ArcGIS by subtracting the original DEM from the filled DEM.

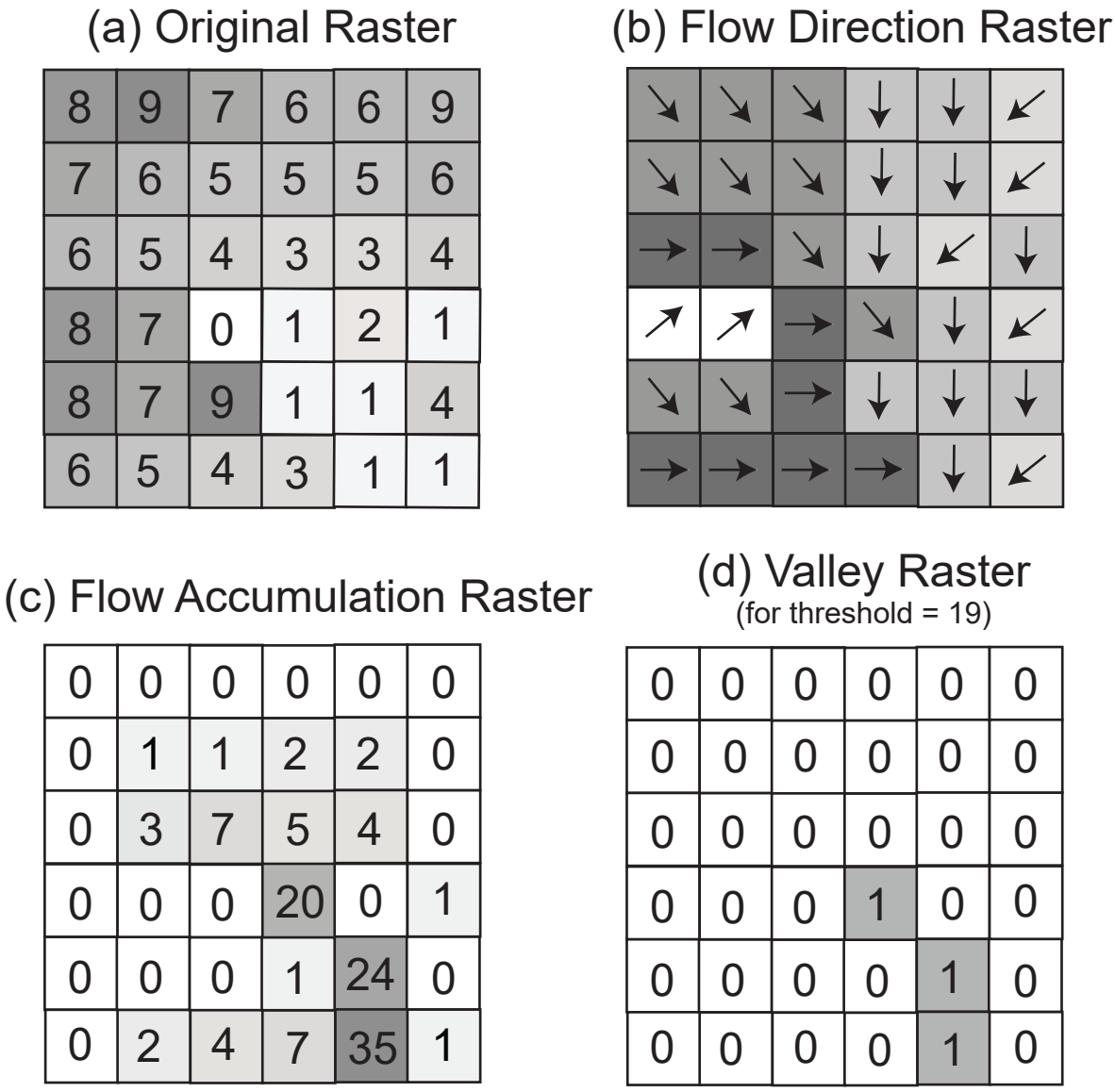

Figure 4: A cartoon representation of the method used for generating the valley systems in this study. a) The original DEM raster. b) The flow direction raster generated using the D8 flow direction algorithm with the Flow Direction tool in ArcMap. Arrows represent the direction to which water will flow and point towards the lowest proximal elevation value. c) The flow accumulation raster generated using the Flow Accumulation tool in ArcMap. Each pixel value represents the number of pixels that would have "flowed through" that pixel. d) A threshold must be chosen for the flow accumulation raster to delineate areas with potential for high water accumulation. In the case of this example the threshold used is 19. Values greater than 19 were changed to a value of 1 whereas values less than or equal to 19 were changed to a value of zero. Pixels with a value of 1 represent the valley system.

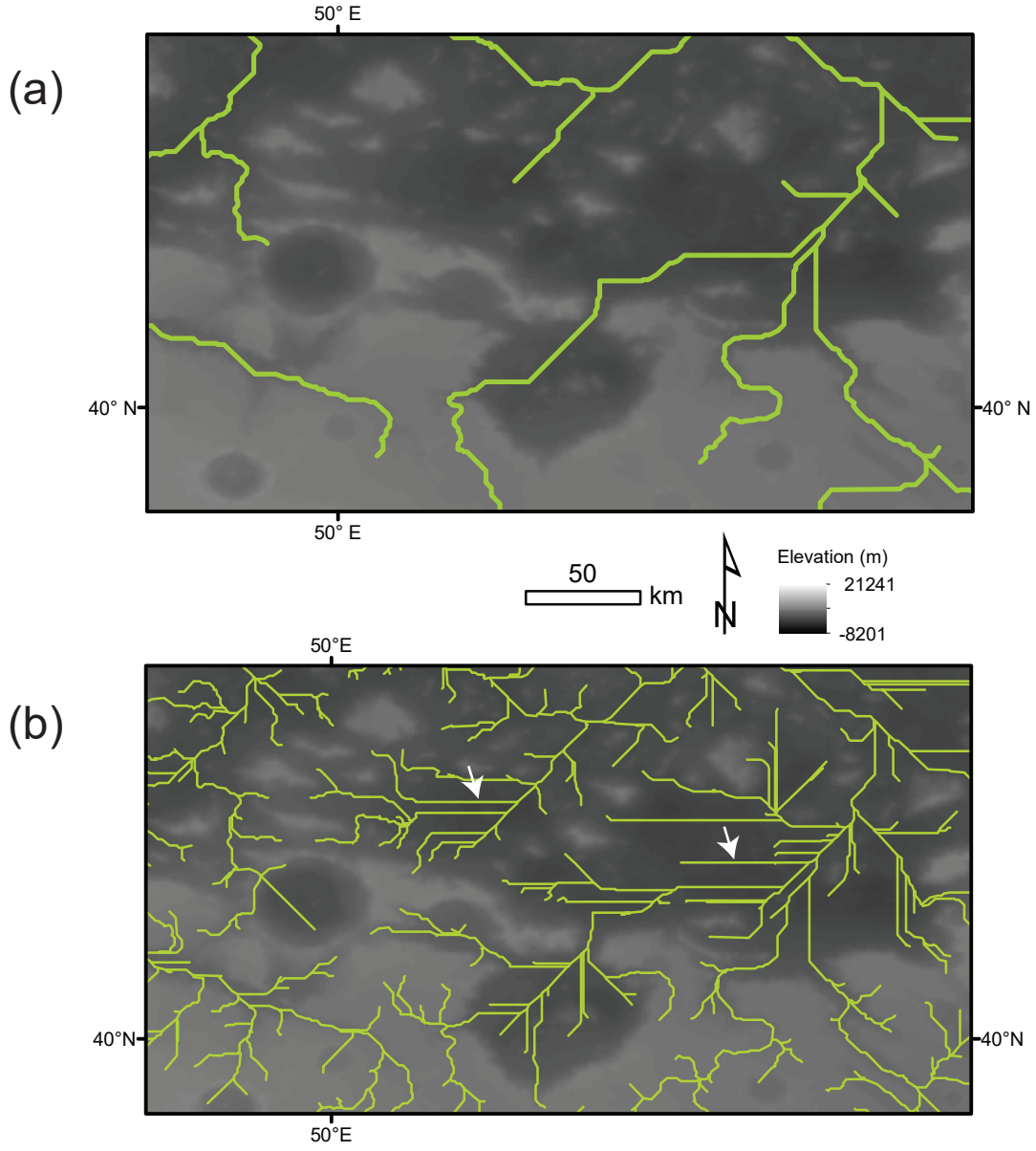

Figure 5: a) A portion of the MOLA DEM within the FT study area. Overlaid in green on the DEM is the mapped valley system generated with the flow accumulation threshold used in this study. b) A portion of the MOLA DEM at the same location as in a. however, overlaid in green is a valley system generated with a lower flow accumulation threshold than used in this study. White arrows point to artifact valleys.

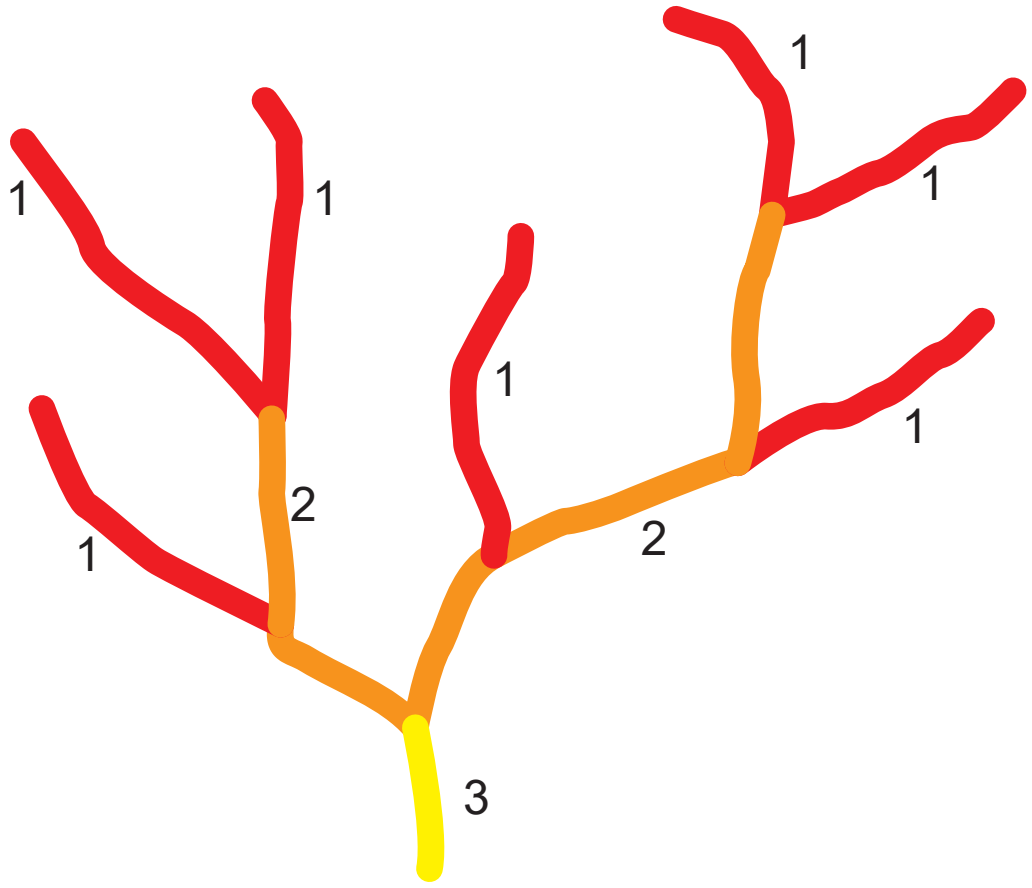

Figure 6: Strahler stream order (Strahler, 1957) characterization. Order 1 streams are in red, order 2 streams are in orange, and order 3 streams are in yellow.

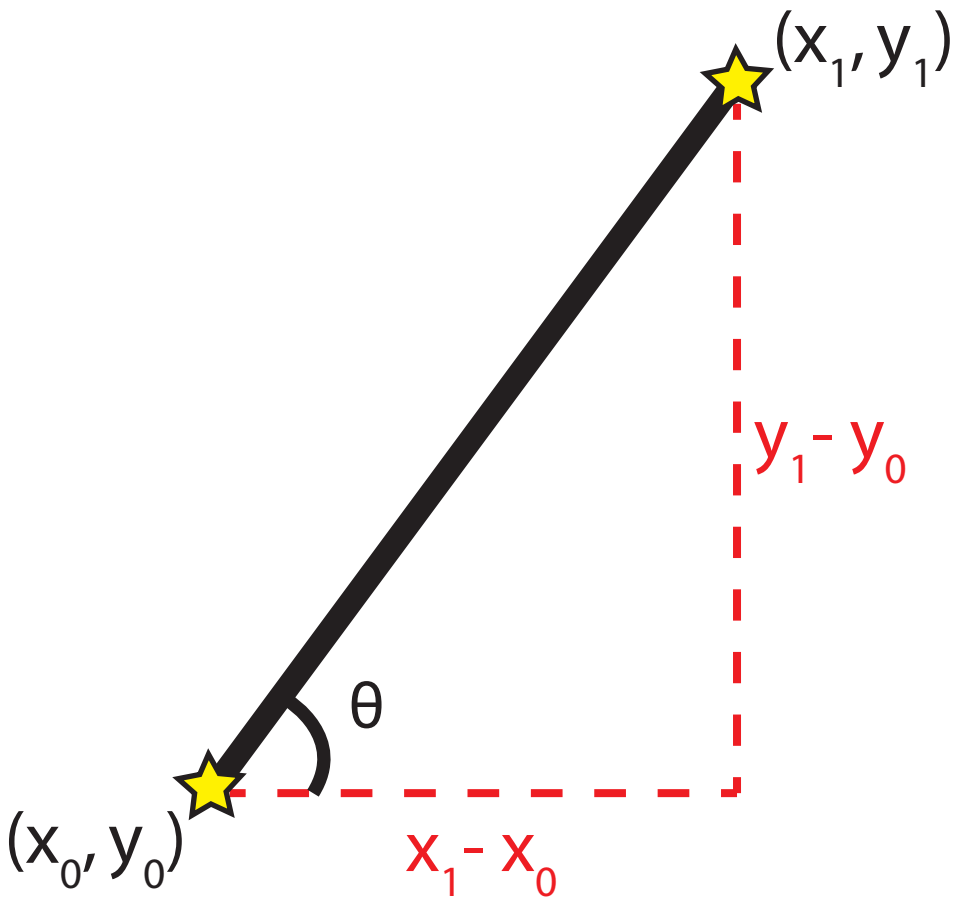

Figure 7: A cartoon representation of the method used for calculating the valley segment azimuths (θ) using Equation 1 in ArcGIS.

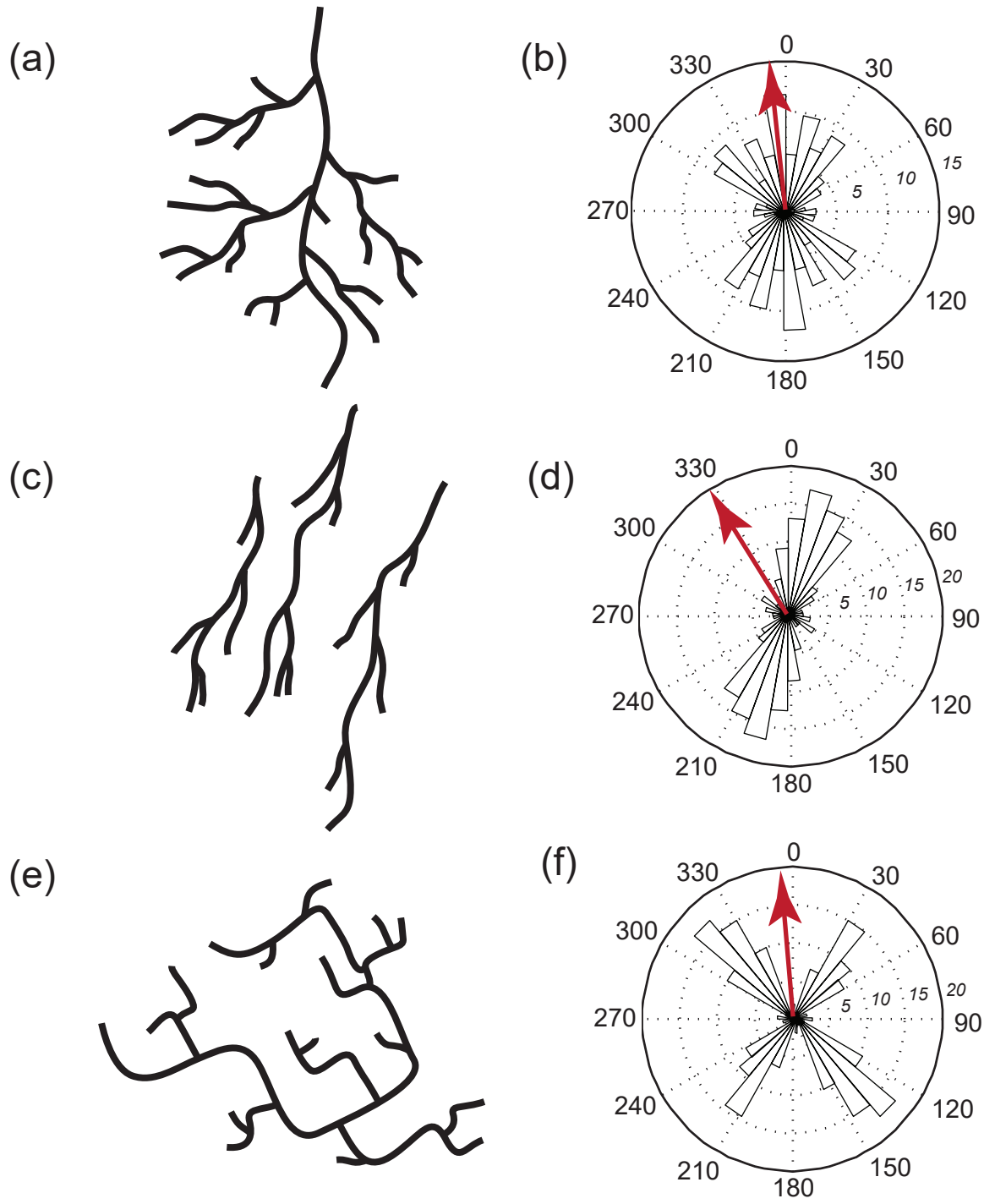

Figure 8: A cartoon representation of primary planform valley geometries: (a) dendritic, (c) parallel, and (e) rectangular (Hugget, 2007) and their corresponding rose diagrams (b,d,f). Italicized numbers and corresponding dashed circles in the rose diagrams correspond to percentages of valley length. The magnitude of each petal is the percentage of valleys that correspond to each azimuth bin.

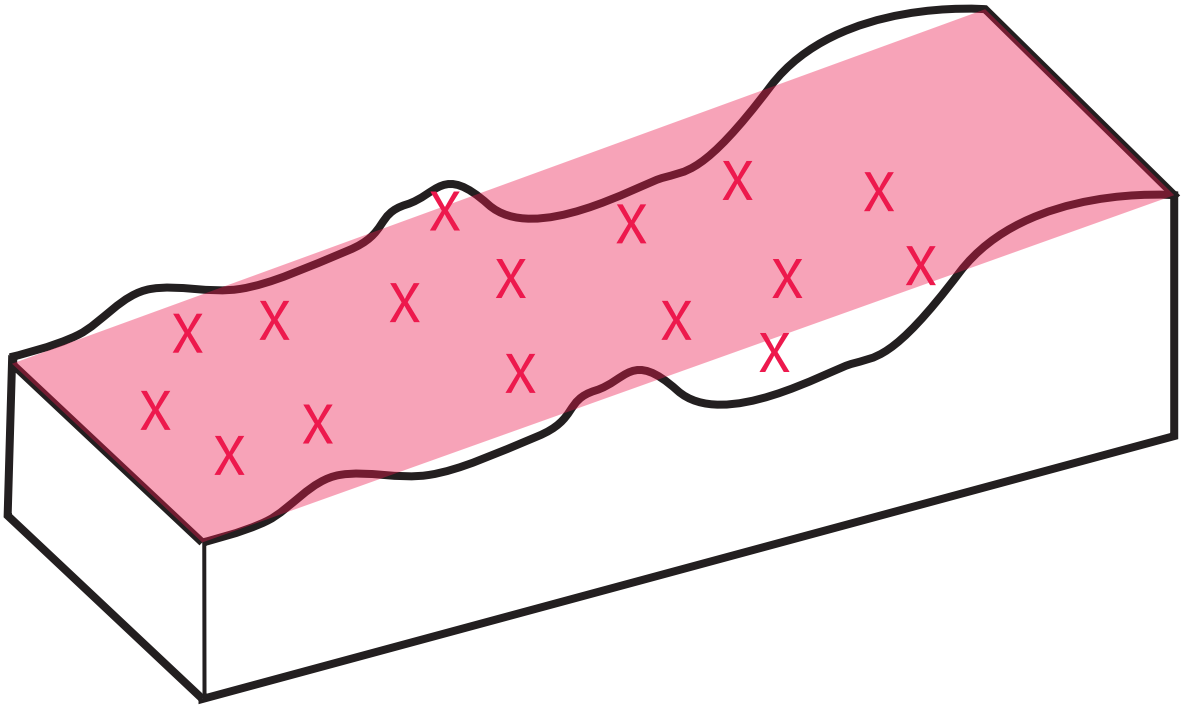

Figure 9: A cartoon representation of the calculation of the downslope direction. Bold line represents the topography (in profile), Red X's represent randomly-chosen elevation values extracted from the topographic data, and the red transparent surface represents the best-fit plane found for the chosen elevation points using a least-squares regression. The slope and aspect of the best-fit plane were computed, and the aspect (map-view direction of the surface normal) was taken as the downslope direction.

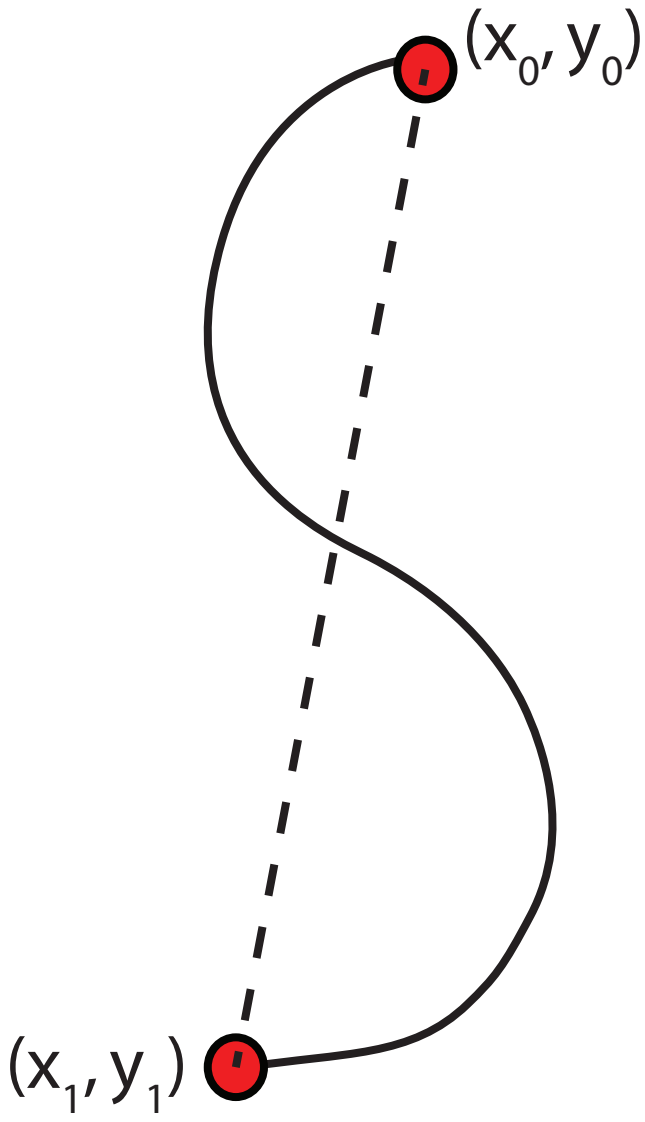

Figure 10: A cartoon representation of the sinuosity calculation. The solid black line represents the valley segment while the dashed line represents the straight distance between the start and end of the segment. By dividing the length of the solid black line by the dashed line you get a sinuosity value. Values greater than 1 indicate more sinuous valley segments while values close to 1 indicate low sinuosity valley segments.

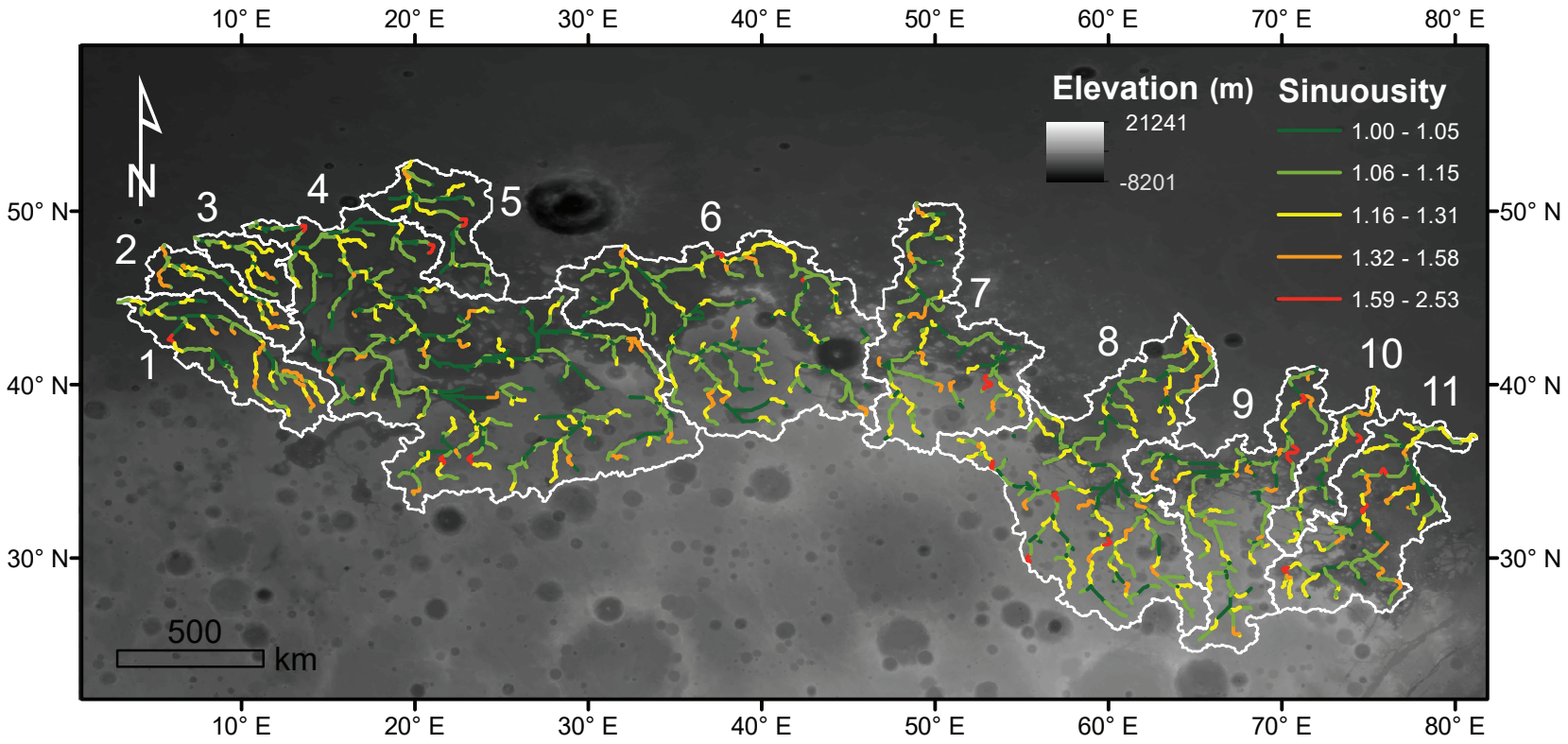

Figure 11: Valley segments colored by their sinuosity values overlaid onto a MOLA DEM. Red colors are more sinuous and indicate a potential fluvial origin while green colors are less sinuous and indicate a potential fracture origin.

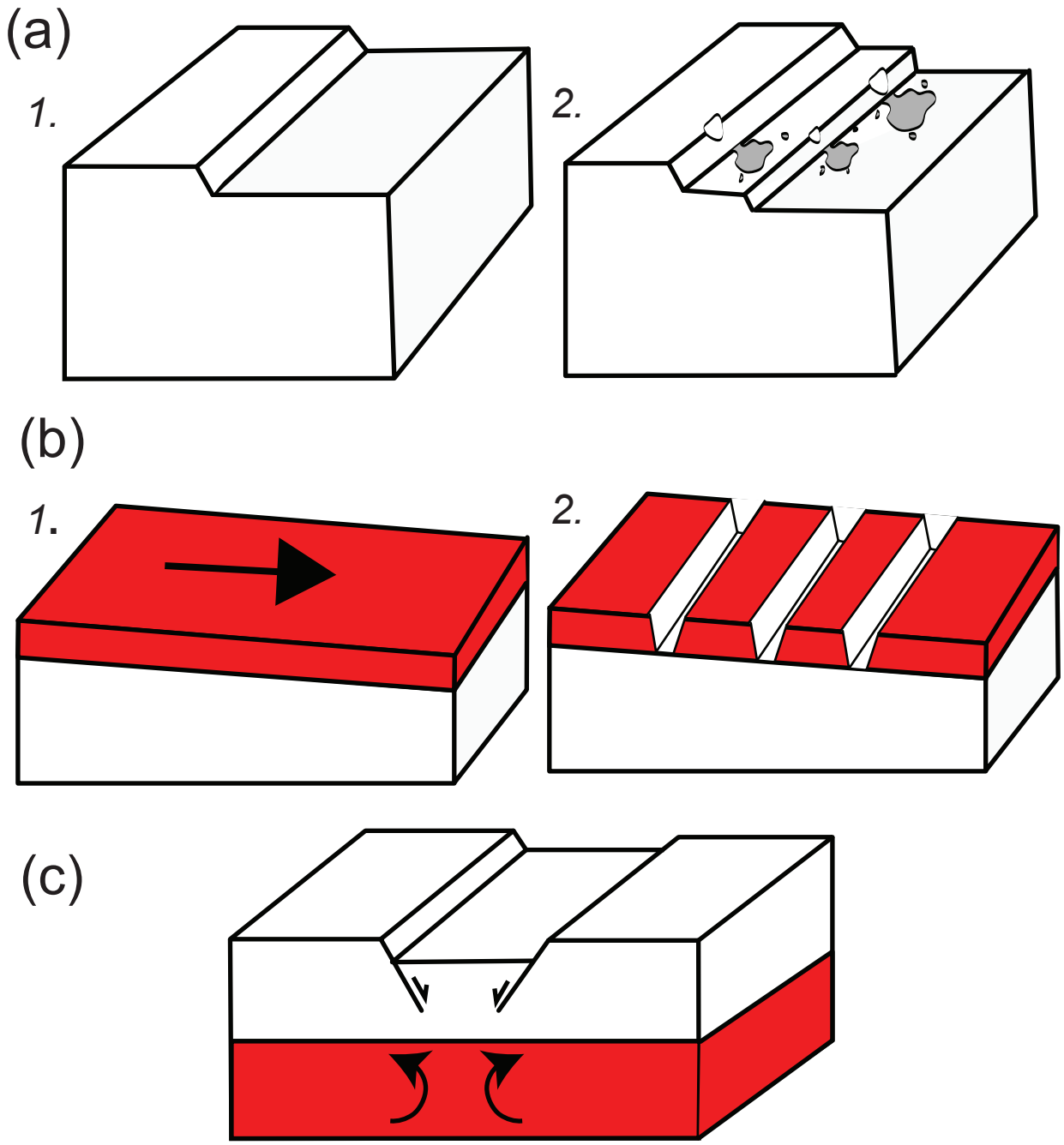

Figure 12: Cartoon representations of three possible scenarios for fracture formation in the FT: a) scarp retreat as proposed by Sharp (1957) where erosion and fracturing (2) is caused by a topographic gradient or preexisting scarp feature (1) b) draping of a massive ignimbrite deposit (red) from local plains-style caldera complexes (1) and subsequent cooling and contracting causing fracturing perpindicular to the topographic gradient (2), c) extension caused by mantle convection during the formation of the dichotomy boundary (Roberts and Zhong, 2006) generating grabens parallel to the dichotomy boundary.

Appendix A: Code for Calculating Valley Azimuths

This appendix contains the code used in this study for calculating valley azimuths. The program was written in Python and VB Script for interfacing with the ArcGIS Field Calculator in ArcGIS version 10.4.1. The inputs for this code are (*x0*, *y0*), the starting coordinates for each valley segment, as well as (*x1*, *y1*), the ending coordinates for each valley segment. First, the arctangent of the difference between *y0* and *y1*, divided by the difference between *x0* and *x1* is calculated and the result is converted from radians to degrees. Then, an if-then statement is used to change the negative values to positive values in order to get azimuths that range between 000 and 180, where 000 is east, 090 is north, and 180 is west. Lastly, cases where the difference between *x0* and *x1* is zero, which would cause the code to return *NaN* due to dividing by zero, are accounted for by changing those values to equal 180.

Calculating Azimuths of Valleys Using Python in ArcGIS Field Calculator

```
# This code calculates azimuths where 0 is east-west and 90 is north-south, put this calculation in a column named "orient"

math.degrees(math.atan(( !y1!- !y0!)/( !x1!- !x0!) ) )

#In a new column named "orienta"

def Reclass(orient):
  if orient < 0:
    return orient + 180
  else:
    return orient

Reclass( !orient!)

VB Script to account for when x0 = x1

# In a new column named "orientb"
# This will be the final calculation for azimuths

Dim orienta
If [x0] = [x1] Then
orientb = 180

else
orientb = [orienta]
end if
```

Appendix B: Code for Classifying Valleys

This appendix contains a Python script to interface with the ArcGIS Field Calculator in ArcGIS version 10.4.1 for categorizing orientation values into 18 classes (1-18). These data are then used for input into the MATLAB code (Appendix D) which generates the rose diagrams.

Python script for classifying orientations in ArcGIS Field Calculator

```
#Where orientb is the orientation resulting from Appendix A


#In a new column


def Reclass(orientb):
    if orientb <= 10:
        return 1
    elif (orientb > 10 and orientb <= 20):
        return 2
    elif (orientb > 20 and orientb <= 30):
        return 3
    elif (orientb > 30 and orientb <= 40):
        return 4
    elif (orientb > 40 and orientb <= 50):
        return 5
    elif (orientb > 50 and orientb <= 60):
        return 6
    elif (orientb > 60 and orientb <= 70):
        return 7
    elif (orientb > 70 and orientb <= 80):
        return 8
    elif (orientb > 80 and orientb <= 90):
        return 9
    elif (orientb > 90 and orientb <= 100):
        return 10
    elif (orientb > 100 and orientb <= 110):
        return 11
    elif (orientb > 110 and orientb <= 120):
        return 12
    elif (orientb > 120 and orientb <= 130):
        return 13
    elif (orientb > 130 and orientb <= 140):
        return 14
    elif (orientb > 140 and orientb <= 150):
        return 15
    elif (orientb > 150 and orientb <= 160):
        return 16
    elif (orientb > 160 and orientb <= 170):
        return 17
    elif (orientb > 170 and orientb <= 180):
        return 18
```

Append C: Values Used to Generate Rose Diagrams

This appendix contains the azimuth data used in the MATLAB code found in Appendix D for generating rose diagrams. These data were generated with Microsoft Excel 2010 using the azimuth and valley length values calculated in ArcGIS version 10.4.1 for each valley segment as described in Appendices A and B.

Table C1: Percentage values for valley lengths in each basin (columns) that fall in each azimuth bin (rows). These values were calculated with Microsoft Excel 2010 and were used for generating the rose diagrams using the MATLAB code in Appendix D. Statistically significant modes are highlighted in yellow. Note that here 000 is north, 090 is east, and 270 is west.

	Basin Number										
Azimuth	**1**	**2**	**3**	**4**	**5**	**6**	**7**	**8**	**9**	**10**	**11**
180 – 170	3.4	4.5	5.3	3.9	7.7	3.7	3.7	3.8	7.4	2.4	1.8
170 – 160	6.1	6.5	0.0	6.5	3.0	3.5	0.0	5.7	7.6	7.9	2.5
160 – 150	8.8	0.1	0.0	3.5	1.4	6.8	9.7	6.8	7.9	4.2	4.9
150 – 140	12.7	9.0	9.0	5.1	4.3	4.9	8.3	7.5	4.6	4.3	7.3
140 – 130	9.3	9.9	10.0	6.4	6.2	10.4	10.0	8.8	4.0	1.1	7.2
130 – 120	6.8	14.0	2.3	4.8	5.8	7.8	3.5	7.0	4.3	3.7	7.0
120 – 110	8.2	16.9	21.4	6.1	7.5	4.6	3.9	3.5	1.5	1.6	6.3
110 – 100	6.8	9.3	30.0	5.8	3.6	6.5	6.6	3.3	2.7	0.0	0.0
100 – 90	6.4	12.8	8.2	9.9	13.5	5.2	3.9	3.1	8.0	4.6	4.8
90 – 80	7.2	3.2	0	12.2	8.8	9.9	5.3	6.3	11.1	10.1	6.0
80 – 70	5.0	2.2	4.8	4.2	4.3	3.7	6.3	6.9	8.3	9.3	8.9
70 – 60	1.2	0.0	0.7	4.3	2.9	6.2	4.3	4.4	2.0	0.9	6.7
60 – 50	2.1	0.0	0.0	4.9	33	4.0	3.3	5.0	1.3	0.0	5.5
50 – 40	1.9	2.5	0.4	7.0	5.2	5.4	6.5	4.7	7.5	13.1	5.0
40 – 30	1.8	1.6	0.0	2.0	8.6	3.6	9.3	7.5	8.4	3.5	7.6
30 – 20	0.8	1.7	6.4	5.3	10	4.2	5.1	3.2	4.7	7.9	4.9
20 – 10	3.6	5.7	0.0	3.3	3.0	4.7	5.0	4.7	3.1	0.0	4.2
10 – 0	7.9	0.1	1.6	4.6	10.0	4.6	5.3	7.7	5.6	25.3	9.3
Mean	5.6	5.6	5.6	5.6	5.6	5.6	5.6	5.6	5.6	5.6	5.6
Std Dev	3.3	5.3	8.2	2.3	3.2	2.0	2.5	1.8	2.8	6.2	2.3
Mean + Std Dev	8.9	10.9	13.8	7.9	8.8	7.6	8.1	7.4	8.4	11.8	7.9

Table C2: Percentage values for valley lengths in each basin (columns) that fall in each azimuth bin (rows) for each Strahler order (columns). These values were calculated with Microsoft Excel 2010 and were used for generating the rose diagrams using the MATLAB code in Appendix D. Statistically significant modes are highlighted in yellow. Note that here 000 is north, 270 is west, and 090 is east.

Azimuth	Basin Number																			
	1			2			3		4					5			6			
	Strahler Order																			
	1	2	3	1	2	3	1	2	1	2	3	4	5	1	2	3	1	2	3	4
180 – 170	6.4	0.0	0.0	0.0	0.0	45.9	0.0	15.0	3.7	6.6	2.7	0.0	2.8	3.3	13.2	10.7	3.4	7.7	0.0	5.4
170 – 160	3.4	12.0	0.0	1.1	7.7	25.7	0.0	0.0	9.6	1.9	5.0	0.8	7.8	0.2	0.0	9.1	4.9	0.3	4.7	0.0
160 – 150	13.5	0.7	13.2	0.2	0.0	0.0	0.0	0.0	4.6	1.7	5.5	0.0	0.0	2.9	0.0	0.0	6.6	12.6	3.1	3.9
150 – 140	11.9	17.6	0.0	20.0	0.0	0.0	13.9	0.0	2.5	0.1	11.0	10	18.7	0.0	0.0	13.6	4.7	2.5	8.1	3.6
140 – 130	10.7	6.8	11.2	11.6	9.9	2.3	15.3	0.0	4.7	9.6	7.2	7.3	5.5	5.0	6.4	8.0	4.5	19.6	7.3	31.7
130 – 120	2.9	12.8	6.3	0	30.9	0.0	0.0	6.4	4.9	0.8	5.5	0.0	18.7	12.2	0.0	0.0	6.5	8.0	7.4	16.5
120 – 110	11.2	6.3	0.0	12.7	19.9	22.3	19.8	24.2	6.8	2.4	11.3	3.2	2.8	6.1	5.6	11.0	5.8	2.8	5.3	0.5
110 – 100	1.0	7.3	34.7	15.2	5.4	0.0	30.6	29.0	8.2	1.8	6.5	7.0	0.0	1.4	13.9	0.0	4.4	6.9	10.5	8.2
100 – 90	3.5	12.8	0.0	12.1	16.3	0.0	0.0	23.3	7.4	10.8	12.2	14.3	15.4	5.8	23.8	18.2	5.9	5.5	6.0	2.3
90 – 80	7.1	6.9	8.7	0.4	6.7	0.0	0.0	0.0	10.9	19.7	5.4	17	10.7	11.3	16.4	0.0	16.3	3.9	50	0.0
80 – 70	0.0	9.4	15.0	4.9	0.0	0.0	7.4	0.0	3.9	4.5	3.5	9.9	2.9	9.1	0.0	0.0	2.5	2.0	9.5	0.0
70 – 60	0.0	0.0	10.9	0.0	0.0	0.0	0.0	2.1	3.1	7.3	7.4	0.0	0.0	6.1	0.0	0.0	4.9	6.2	11.8	0.0
60 – 50	3.9	0.0	0.0	0.0	0.0	0.0	0.0	0.0	5.1	7.3	4.0	3.8	0.0	2.5	3.0	4.6	5.2	0.0	6.5	0.0
50 – 40	0.2	5.1	0.0	2.3	3.1	0.0	0.6	0.0	5.2	9.3	2.5	21.2	10.3	8.4	1.2	3.1	4.8	7.0	4.0	8.2
40 – 30	3.2	0.2	0.0	3.6	0.0	0.0	0.0	0.0	3.1	1.1	1.7	0.0	0.0	11.3	3.6	7.9	3.1	8.5	1.4	0.0
30 – 20	0.0	2.1	0.0	2.9	0.0	3.8	9.9	0.0	7.5	5.7	2.2	0.0	1.1	1.6	0.0	0.7	5.4	5.3	2.3	0.0
20 – 10	6.7	0.0	0.0	12.8	0.0	0.0	0.0	0.0	3.0	5.5	2.1	5.5	0.0	6.3	0.0	0.0	6.2	0.9	3.2	8.2
10 – 0	14.7	0.0	0.0	0.2	0.0	0.0	2.5	0.0	5.8	4.1	4.1	0.0	3.5	6.6	12.8	13.2	5.5	0.1	4.0	11.5
Mean + Stdev	10.5	11.1	14.7	12.1	14.3	18.2	14.5	15.5	7.9	10.4	8.8	12.2	12.1	9.4	12.9	11.5	8.4	10.5	8.7	13.7

Table C2 <continued>

Azimuth	Basin Number																
	7				8				9			10		11			
	Strahler Order																
	1	2	3	4	1	2	3	4	1	2	3	1	2	1	2	3	4
180 – 170	5.3	5.3	0.0	0.0	5.2	1.8	8.9	0.0	6.4	6.9	10.7	0.0	3.7	1.7	0.0	4.4	0.0
170 – 160	0.0	0.0	0.0	0.0	3.7	9.0	3.7	7.4	10.0	8.5	0.0	12.8	5.4	3.7	0.0	0.0	7.0
160 – 150	11.7	5.3	0.0	21.3	6.9	9.1	0.0	4.7	9.2	9.8	1.7	12.6	0.0	4.1	9.1	5.2	0.0
150 – 140	6.7	16.7	0.0	8.6	6.6	14.5	0.5	0.0	6.6	4.0	0.0	12.8	0.0	5.2	16.6	7.5	0.0
140 – 130	4.3	14.3	20.7	10.1	9.3	9.0	11.7	4.7	3.2	4.2	6.1	3.3	0.0	4.9	7.3	9.8	12.6
130 – 120	3.6	0.0	7.9	4.2	9.6	5.0	10.7	0.0	3.8	6.5	2.6	11.0	0.0	10.3	10.9	0.0	0.0
120 – 110	5.9	0.5	0.0	7.2	2.5	3.1	4.1	7.7	0.9	4.0	0.0	4.8	0.0	6.8	2.1	5.8	12.6
110 – 100	8.4	5.2	9.1	0.0	3.9	0.7	8.2	4.0	0.6	8.6	0.0	0.0	0.0	0.0	0.0	0.0	0.0
100 – 90	2.1	9.5	0	4.7	3.4	3.7	0	2.7	9.7	7.9	3.8	12.3	0.7	8.3	4.2	0	0
90 – 80	5.2	7.1	7.9	0.0	4.5	3.1	18.6	13.4	17.2	3.2	5.4	4.5	13.0	3.5	0.0	11.7	16.3
80 – 70	9.4	0.0	0.0	13.5	10.3	0.0	0.0	12.8	3.9	7.6	21.1	6.3	10.9	5.4	7.3	18.7	6.7
70 – 60	3.3	0.0	17.5	0.0	5.5	1.4	9.0	4.6	0.9	2.6	4.0	2.7	0.0	11.0	0.0	0.0	12.6
60 – 50	0.6	7.5	7.9	0.0	55	4.5	0.0	6.7	2.4	0.0	0.0	0.0	0.0	9.4	0.0	3.9	0.0
50 – 40	10.4	2	7.2	0.0	3.0	4.3	11.1	8.8	9.8	0.5	10.7	16.8	11.2	0.3	13.6	2.3	18.2
40 – 30	12.3	8.5	5.5	4.9	8.0	9.5	0.7	5.2	6.5	1.7	22.6	0.0	5.3	8.9	7.3	5.7	6.8
30 – 20	2.6	4.1	5.8	14.4	1.4	5.2	2.8	5.5	4.5	8.7	0.0	0.0	11.9	4.7	0.0	11.6	0.0
20 – 10	2.6	9.5	0.0	10.9	6.6	3.2	0.0	3.4	2.3	3.2	5.4	0.0	0.0	4.2	11.9	0.0	0.0
10 – 0	5.5	4.5	10.4	0.2	4.1	13.0	9.9	8.5	2.1	12.2	6.0	0.0	38.0	7.7	9.6	13.5	7.2
Mean + Stdev	9.2	10.5	11.9	12.0	8.1	9.7	11.1	9.4	9.9	9.0	12.4	11.4	15.0	8.8	11.1	11.2	12.0

Appendix D: Code for Generating Rose Diagrams

This appendix contains MATLAB code for generating rose diagrams with the data obtained from Excel in Appendix C. MATLAB version R2012a was used along with the Mapping Toolbox V3.5. First, a list of 18, evenly-spaced azimuth values between 10 and 180 are converted from degrees to radians. Then, the percentages of valleys corresponding to each azimuth category are listed for each basin. The data for each basin should be copy and pasted into the `y` variable, one at a time. The program then uses the percentage values to duplicate the corresponding radian value as many times as the percentage value indicates. For example, a percentage value of 7 results in repetition of the associated radian value 7 times. Finally, the code places the concatenated list of radian values into the `x` variable, and a rose diagram is generated using the `rose` command with 36 as the number of bins. The number 36 is used because the valley azimuths were originally separated by 10 degrees and 360/10 is 36.

MATLAB Code for generating rose diagrams

```
% roses.m

clc
clear

% creating a list of 10 - 180 degrees by 10 in radians(bins)
z = [deg2rad(9) deg2rad(19) deg2rad(29) deg2rad(39) deg2rad(49)
deg2rad(59) deg2rad(69) deg2rad(79) deg2rad(89) deg2rad(99)
deg2rad(109) deg2rad(119) deg2rad(129) deg2rad(139) deg2rad(149)
deg2rad(159) deg2rad(169) deg2rad(179)];

% percents of segmented valleys from excel in 18 bins for each basin
(1-11)
basin1 = [7 5 1 2 2 2 1 4 8 3 6 9 13 9 7 8 7 6];
basin2 = [3 2 0 0 3 2 2 6 0 5 7 0 9 10 14 17 9 13];
basin3 = [0 5 1 0 0 0 6 0 2 5 0 0 9 10 2 21 30 8];
basin4 = [12 4 4 5 7 2 5 3 5 4 7 4 5 6 5 6 6 10];
basin5 = [9 4 3 3 5 9 1 3 10 8 3 1 4 6 6 8 4 14];
basin6 = [10 4 6 4 5 4 4 5 5 4 4 7 5 10 8 5 7 5];
basin7 = [5 6 4 3 7 9 5 5 5 4 0 10 8 10 4 4 7 4];
basin8 = [6 7 4 5 5 8 3 5 8 4 6 7 8 9 7 4 3 3];
basin9 = [11 8 2 1 8 8 5 3 6 7 8 8 5 4 4 2 3 8];
basin10 = [10 9 1 0 13 4 8 0 25 2 8 4 4 1 4 2 0 5];
basin11 = [6 9 7 6 5 8 5 4 9 2 3 5 7 7 7 6 0 5];

y = []; %put list of numbers from above that you want to make a rose
diagram for here

%empty matrix for adding to
x = [];

% loop for creating list to use for generating the rose diagram
for s = 1:18
    % repeat the corresponding radian value the number of times from y
    m = repmat(z(s),1,y(s));
    % concatenate onto list
    x = cat(2,x,m);
    %loop
    s = s+1;
end

%make rose diagram from generated list
rose(x,36);
```

Appendix E: Valleys and Basins Generated in this Study

This appendix contains 11 figures, one for every drainage basin investigated in this study. Each figure displays the drainage basin polygons and valley vectors generated with ArcGIS version 10.4.1. Valleys are colored by Strahler order.

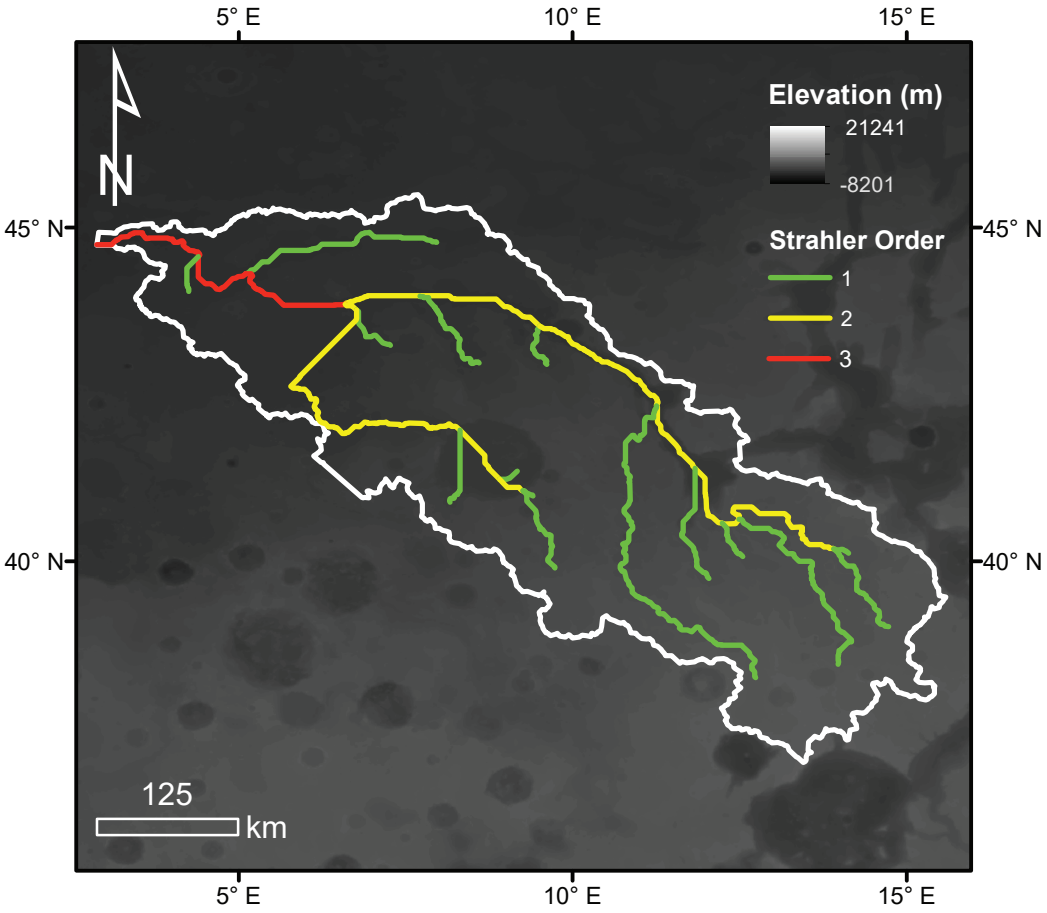

Figure E1: Drainage basin (white) and valleys generated with the D8 flow direction algorithm for basin 1, colored by Strahler order.

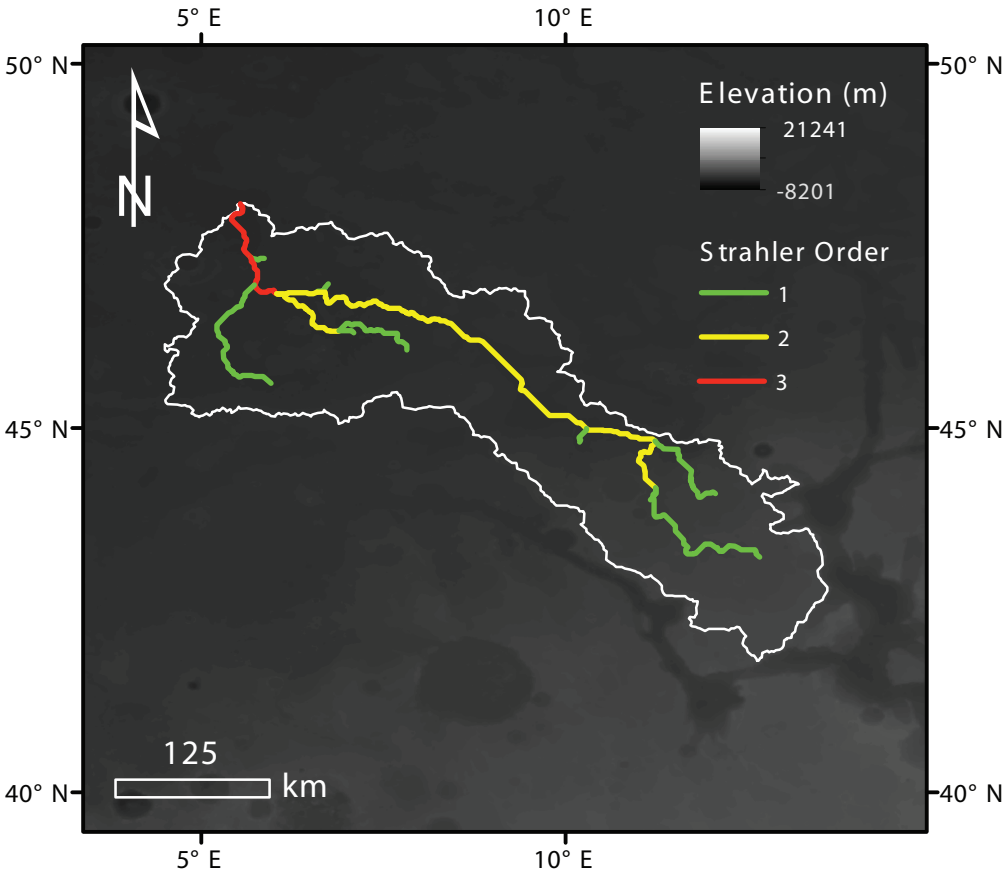

Figure E2: Drainage basin (white) and valleys generated with the D8 flow direction algorithm for basin 2, colored by Strahler order.

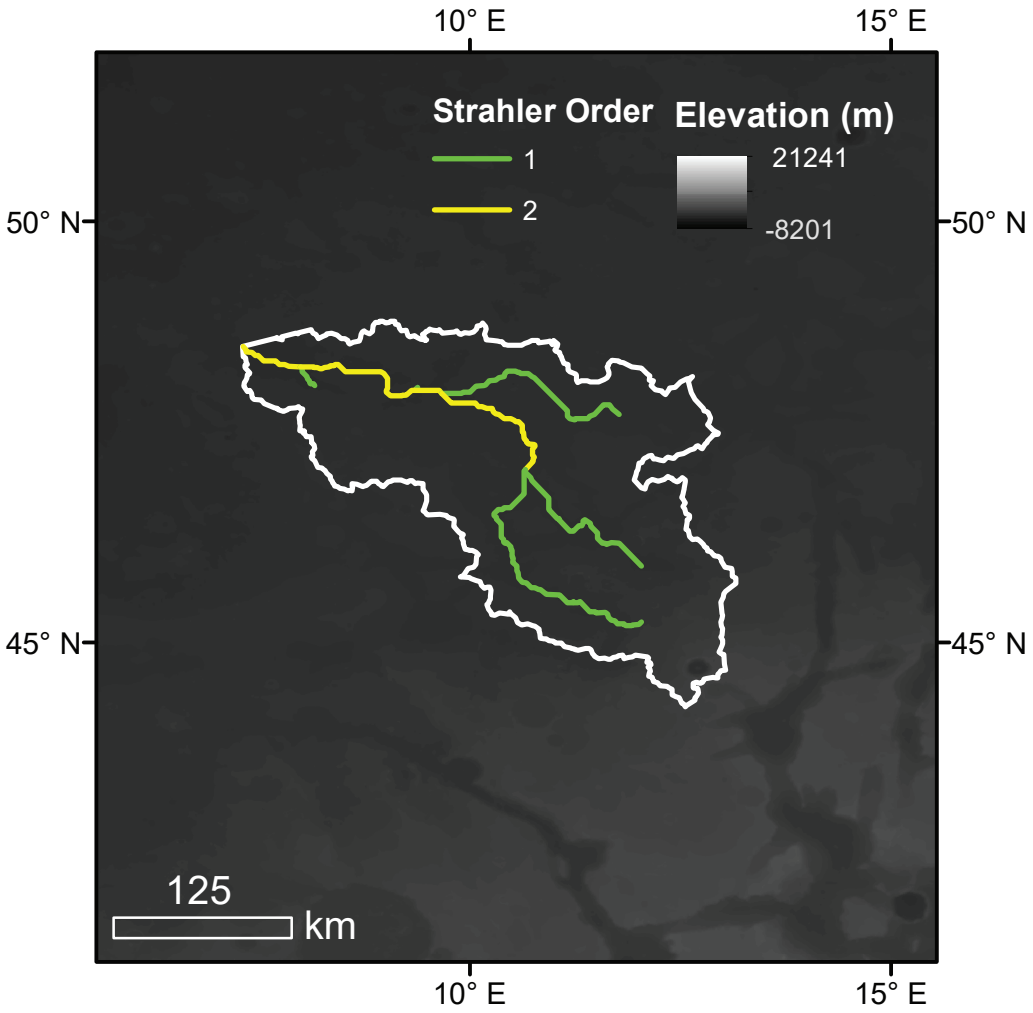

Figure E3: Drainage basin (white) and valleys generated with the D8 flow direction algorithm for basin 3, colored by Strahler order.

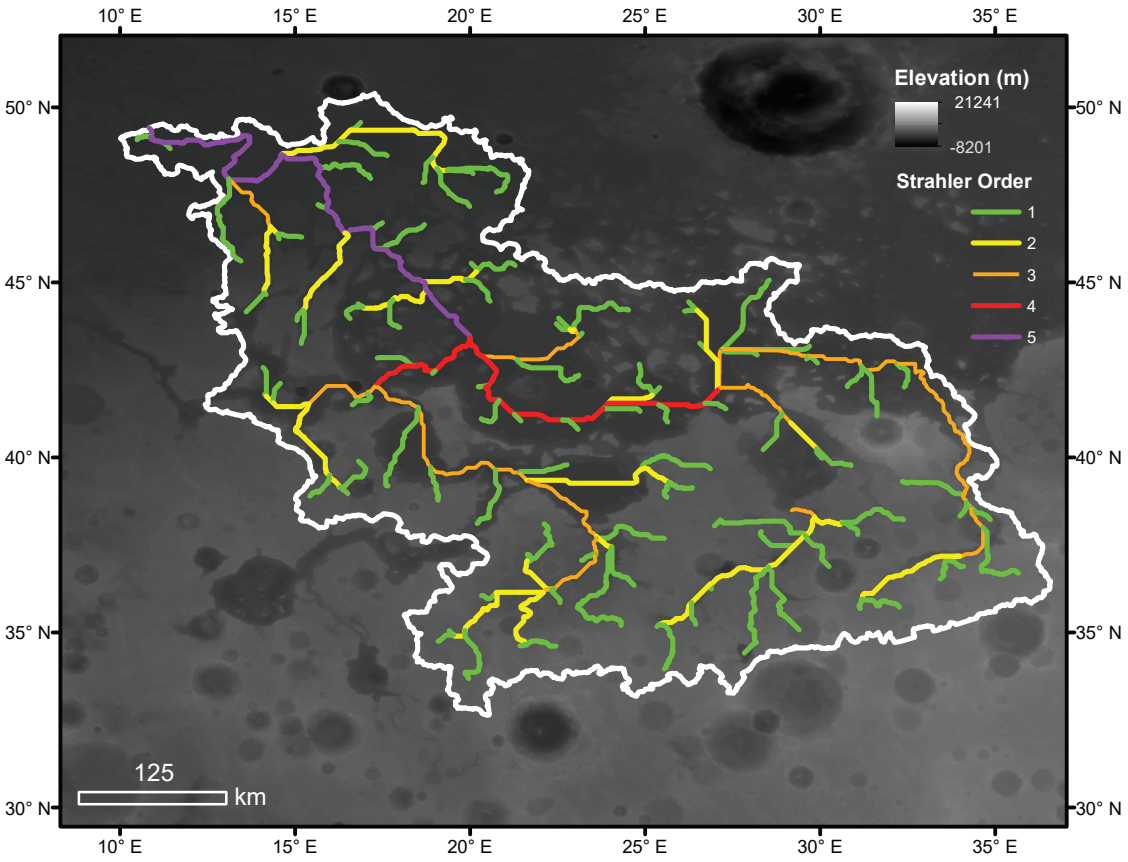

Figure E4: Drainage basin (white) and valleys generated with the D8 flow direction algorithm for basin 4, colored by Strahler order.

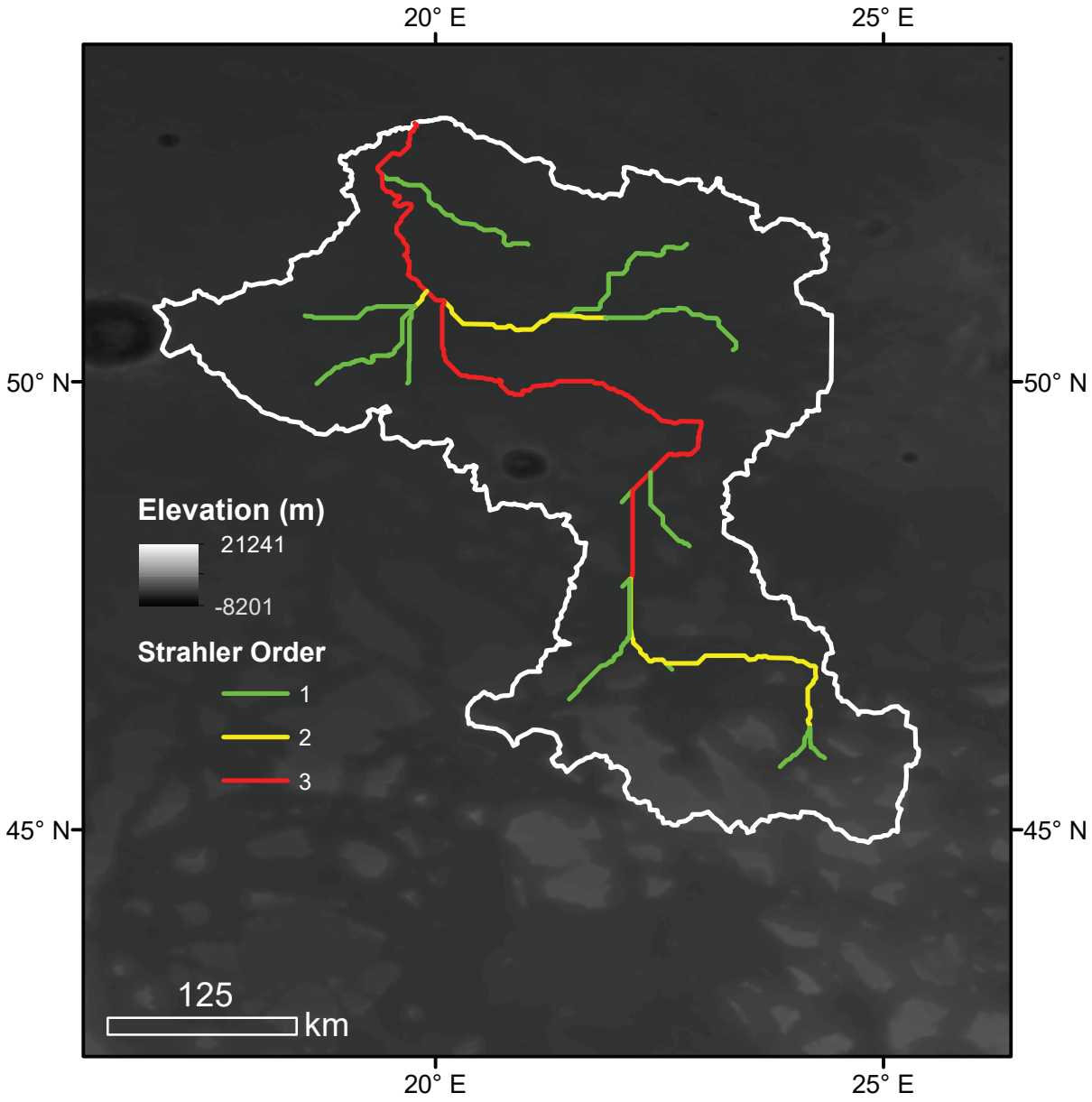

Figure E5: Drainage basin (white) and valleys generated with the D8 flow direction algorithm for basin 5, colored by Strahler order.

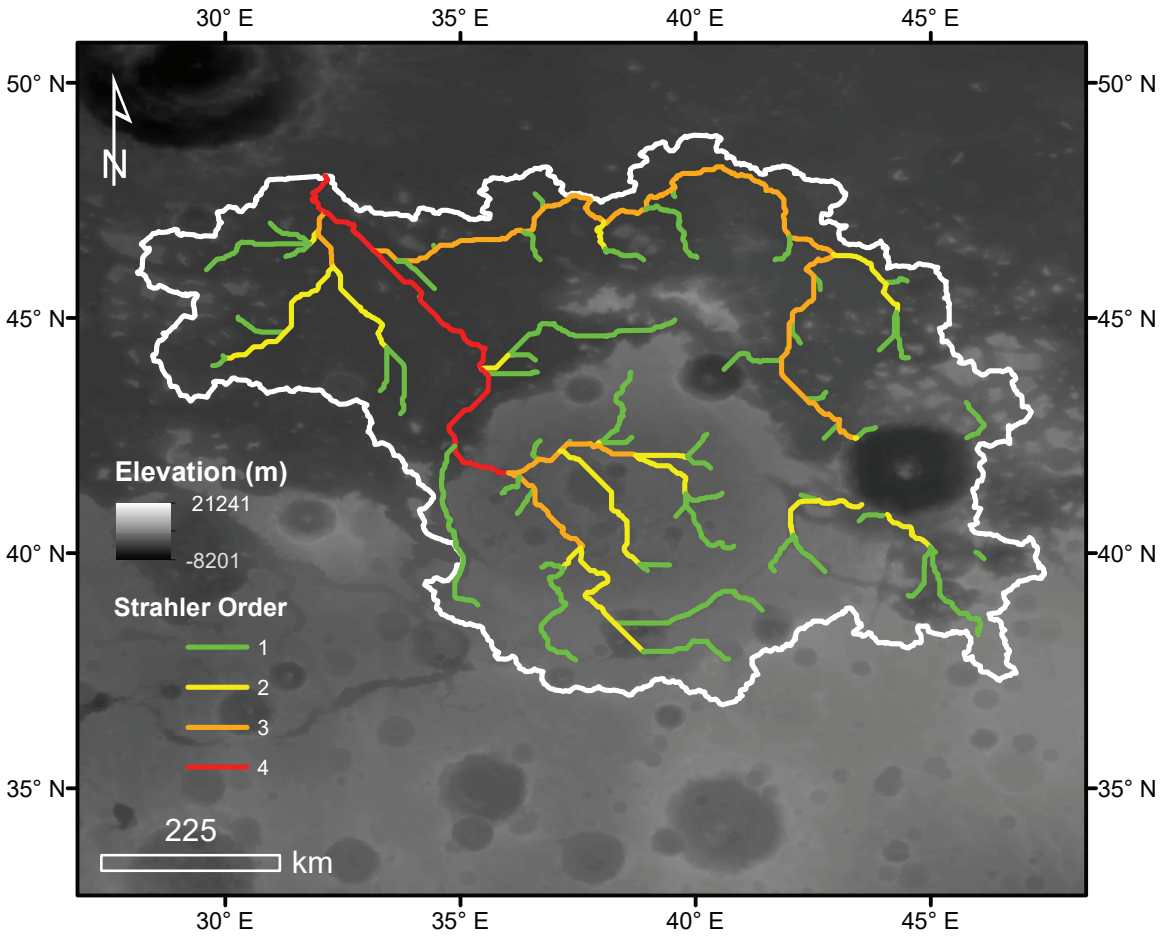

Figure E6: Drainage basin (white) and valleys generated with the D8 flow direction algorithm for basin 6, colored by Strahler order.

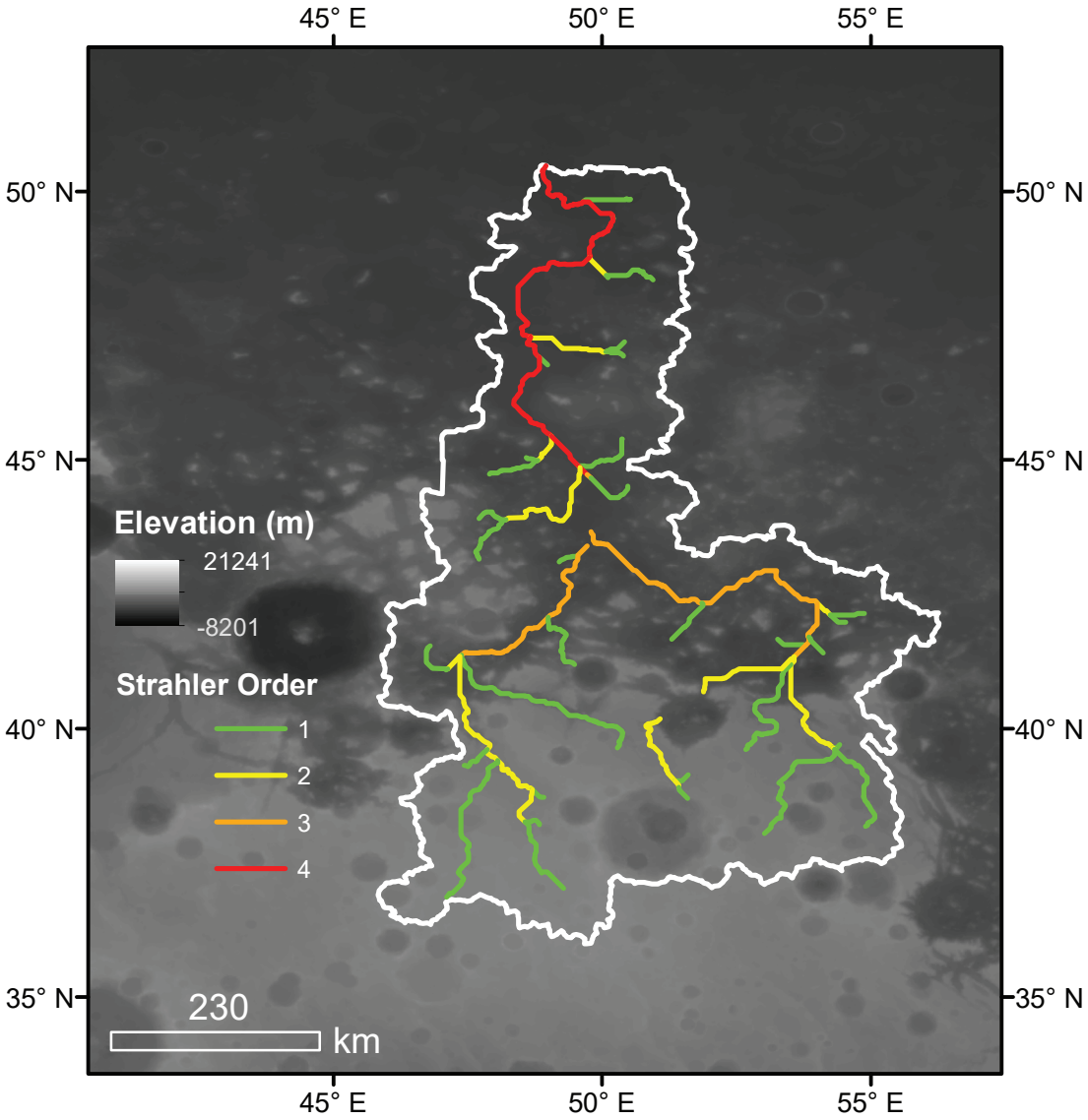

Figure E7: Drainage basin (white) and valleys generated with the D8 flow direction algorithm for basin 7, colored by Strahler order.

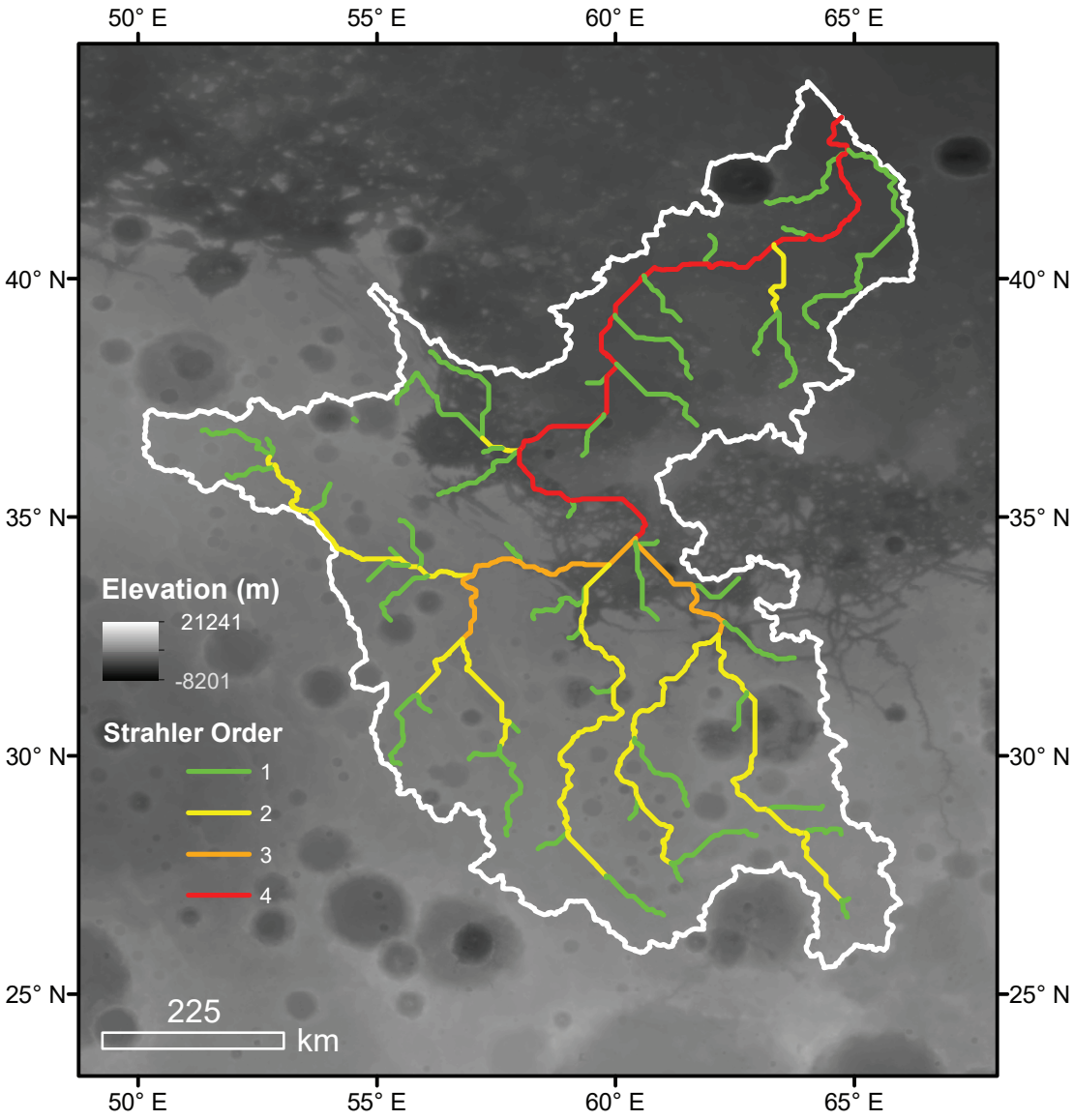

Figure E8: Drainage basin (white) and valleys generated with the D8 flow direction algorithm for basin 8, colored by Strahler order.

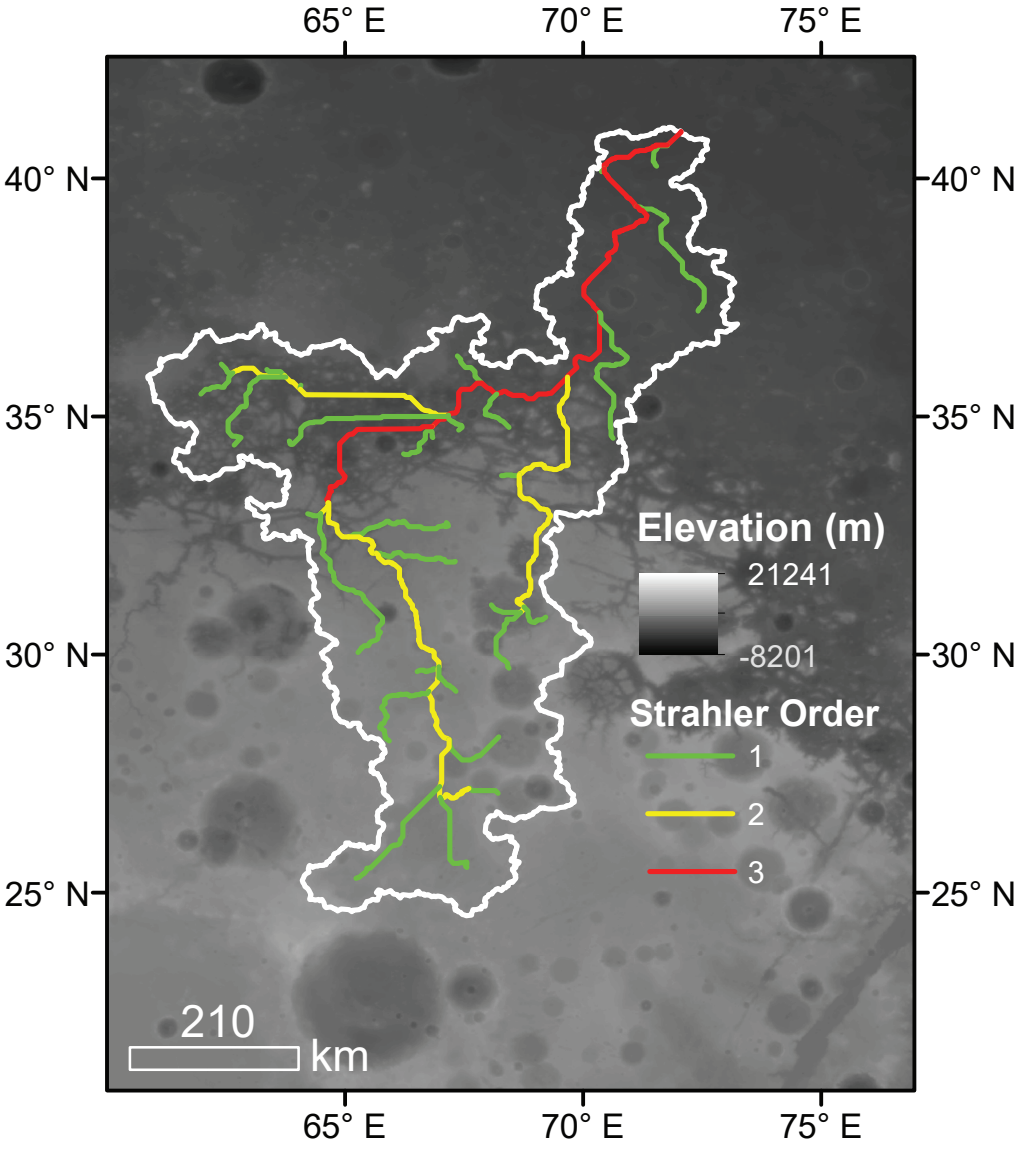

Figure E9: Drainage basin (white) and valleys generated with the D8 flow direction algorithm for basin 9, colored by Strahler order.

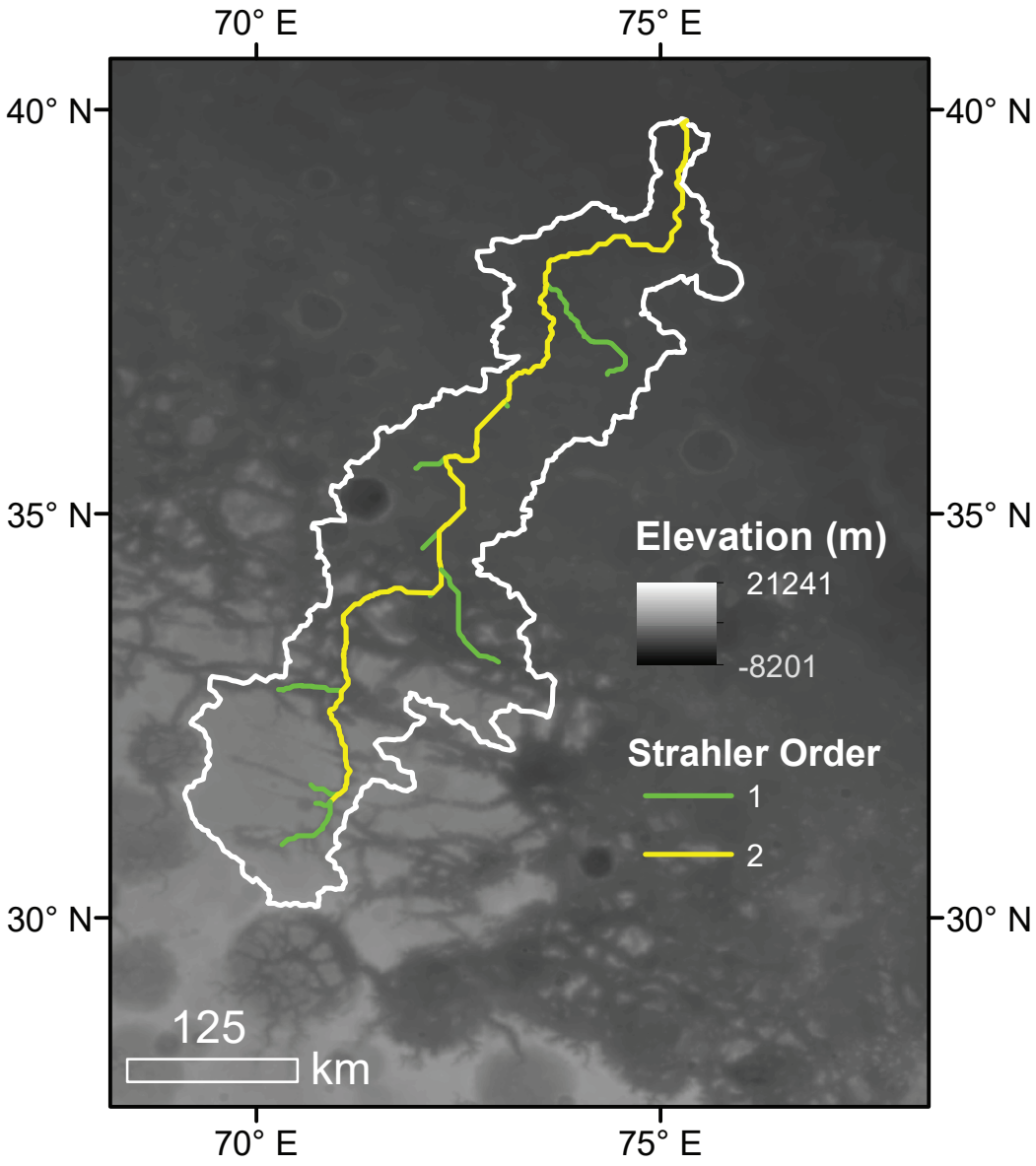

Figure E10: Drainage basin (white) and valleys generated with the D8 flow direction algorithm for basin 10, colored by Strahler order.

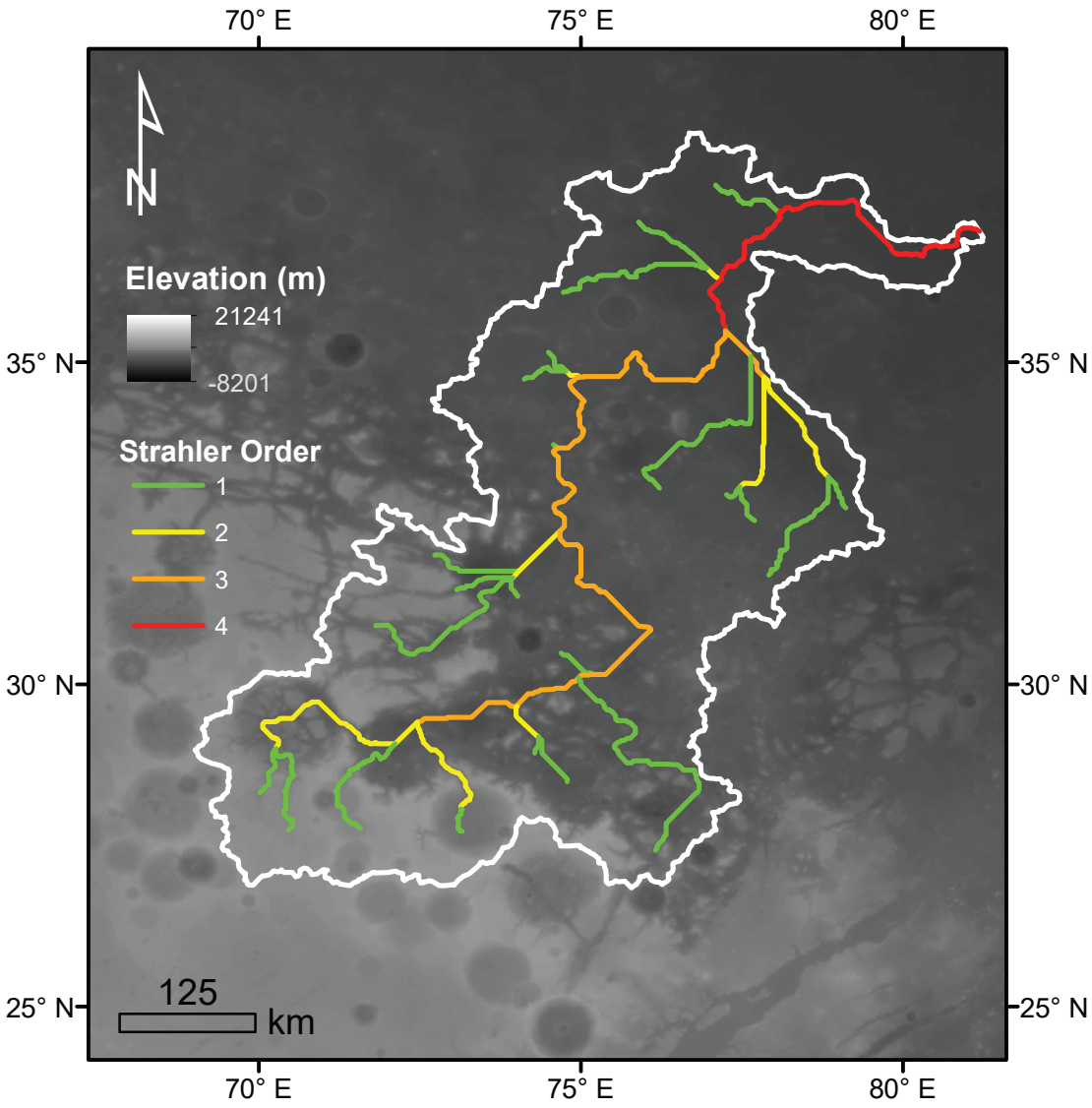

Figure E11: Drainage basin (white) and valleys generated with the D8 flow direction algorithm for basin 11, colored by Strahler order.

Appendix F: Rose Diagrams for Valleys

This appendix contains 11 figures, one for each basin investigated in this study, with rose diagrams of valley segments classified by Strahler order. Italicized numbers and corresponding dashed circles in the rose diagrams correspond to percentages of valley length. The magnitude is the percentage of valleys that correspond to each azimuth bin. The black, dashed circle represents "$\mu+1\sigma$" threshold for which values above would be considered statistically significant. Grey petals in the rose digram represent statistically significant modes.

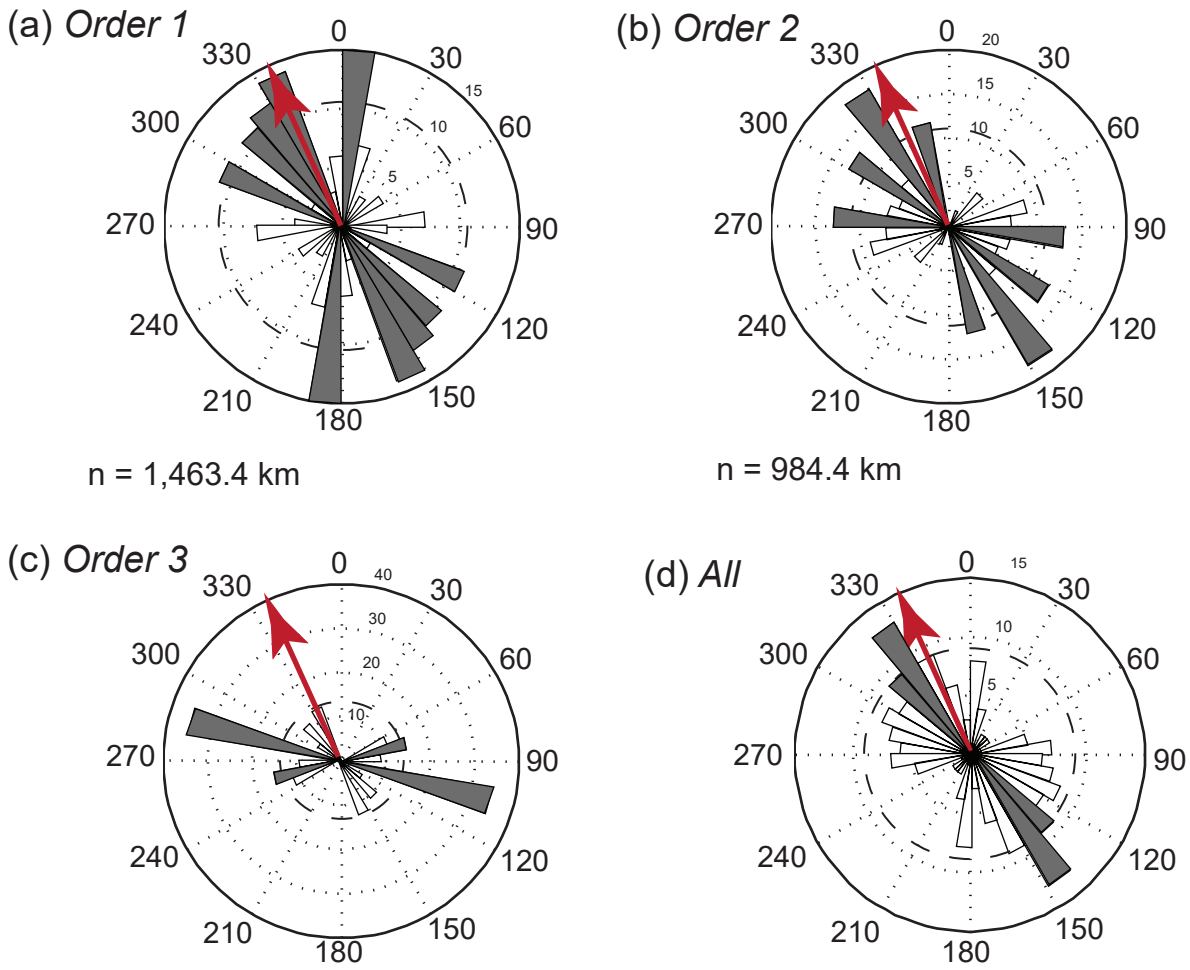

Figure F1: Rose diagrams for basin 1 for all valley segments and Strahler order 1, 2 and 3.

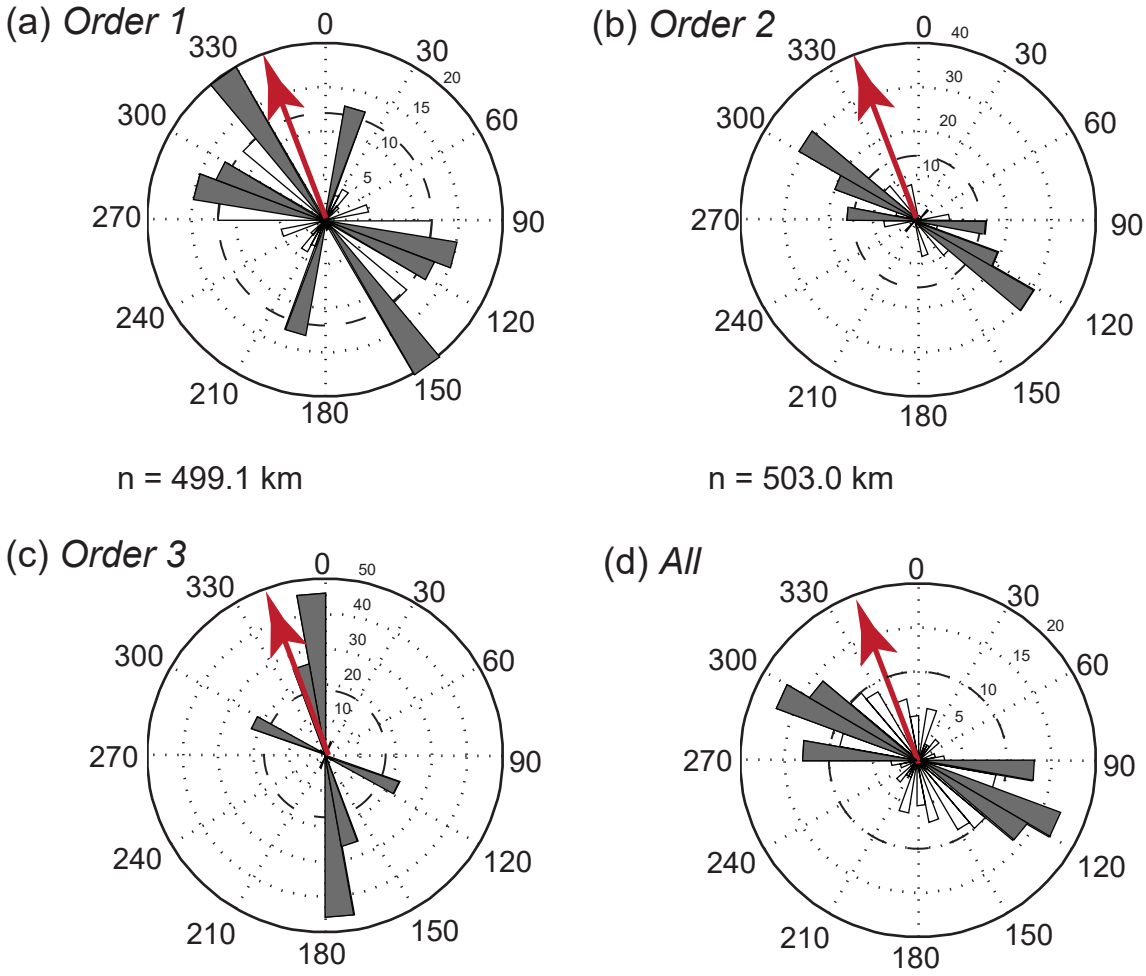

Figure F2: Rose diagrams for basin 2 for all valley segments and Strahler order 1, 2 and 3.

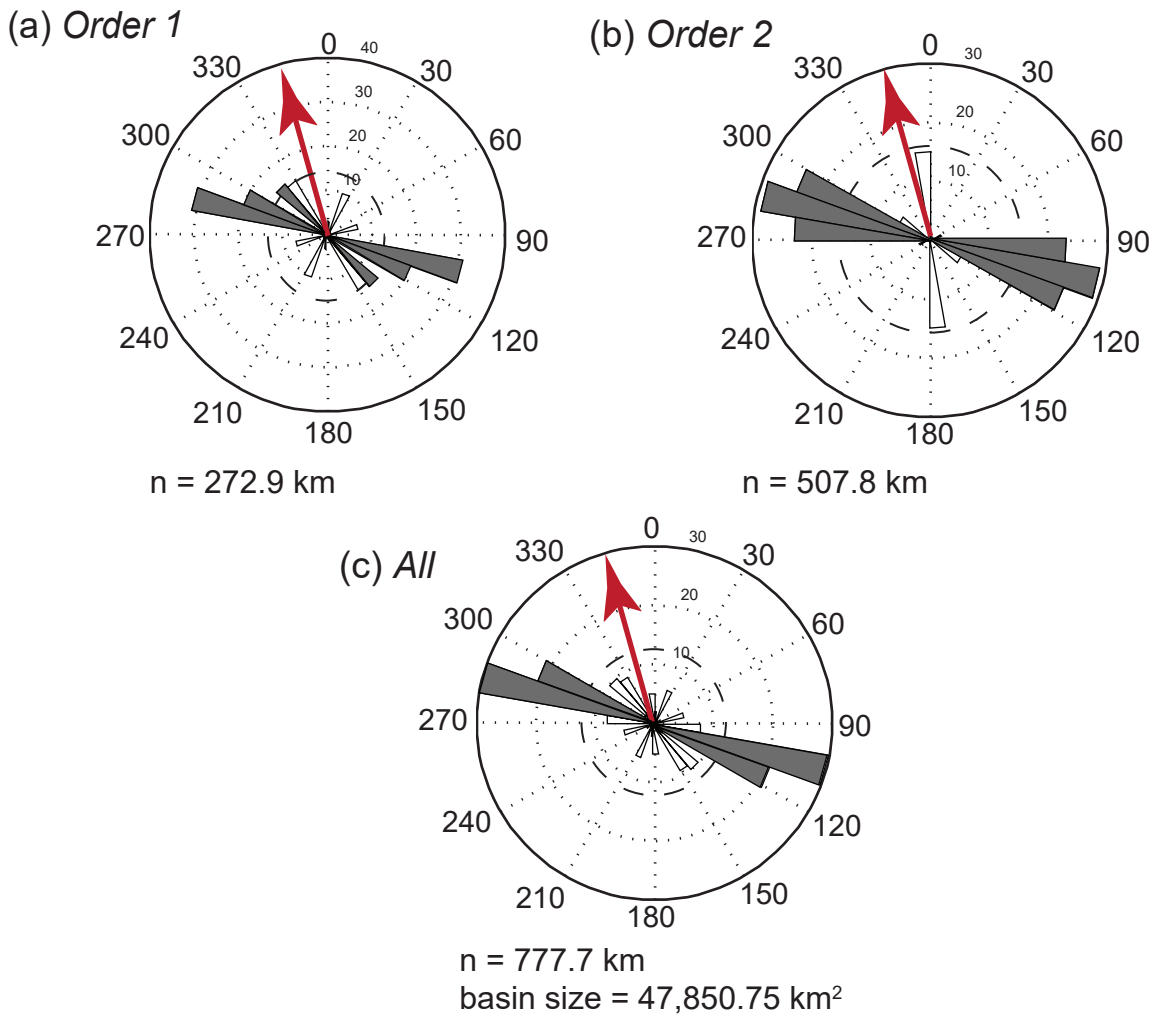

Figure F3: Rose diagrams for basin 3 for all valley segments and Strahler order 1 and 2.

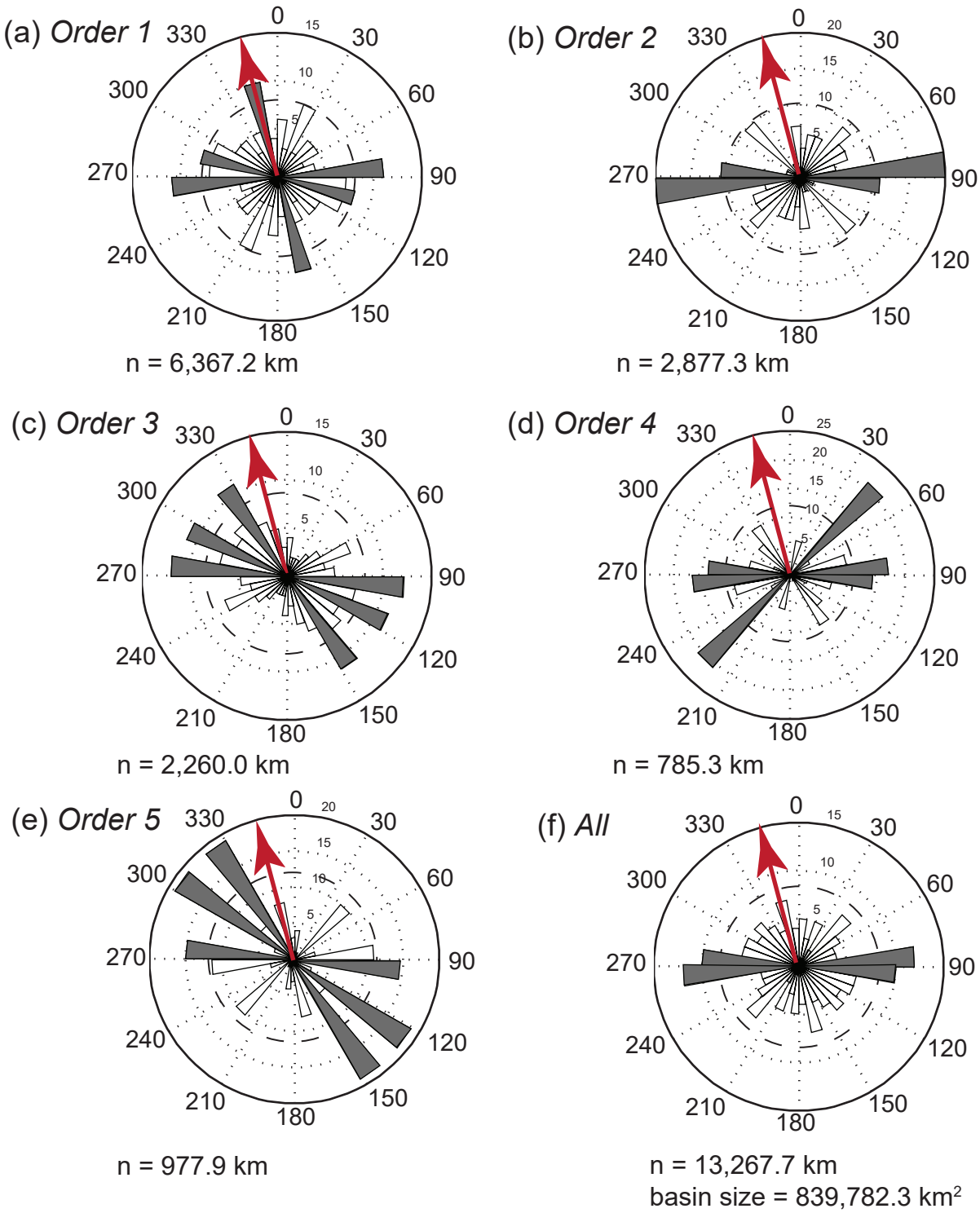

Figure F4: Rose diagrams for basin 4 for all valley segments and Strahler order 1, 2, 3, 4 and 5.

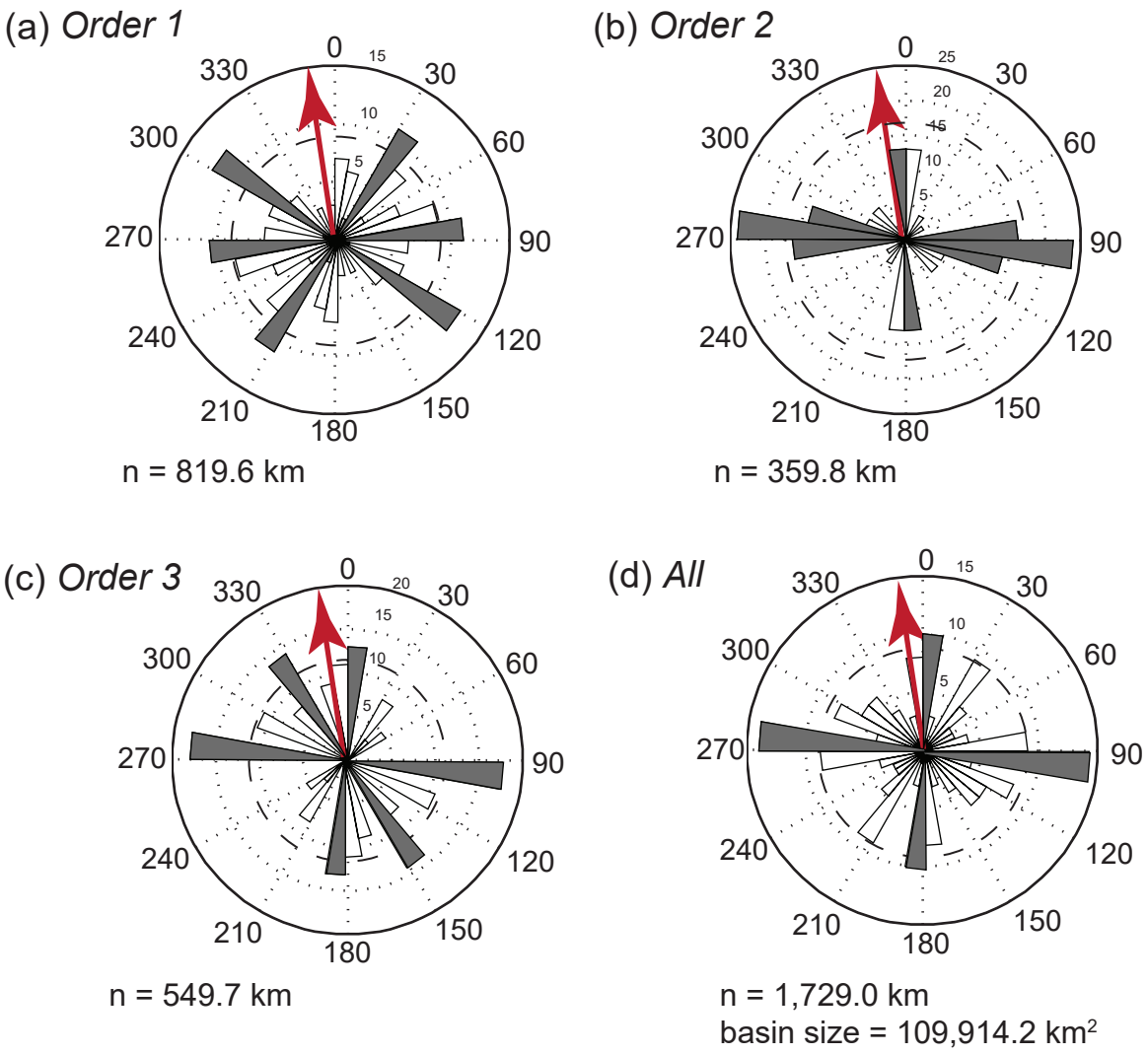

Figure F5: Rose diagrams for basin 5 for all valley segments and Strahler order 1, 2 and 3.

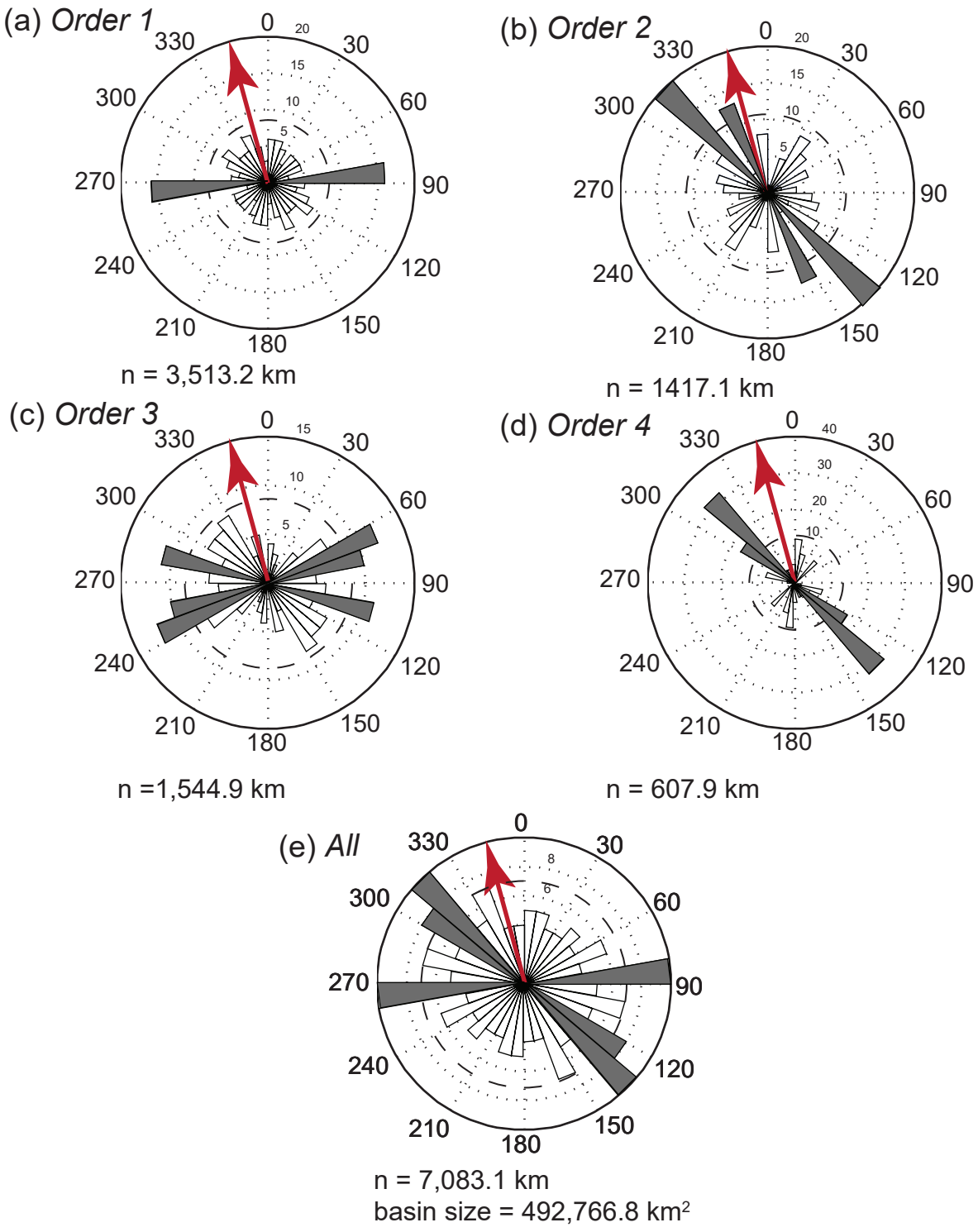

Figure F6: Rose diagrams for basin 6 for all valley segments and Strahler order 1, 2, 3 and 4.

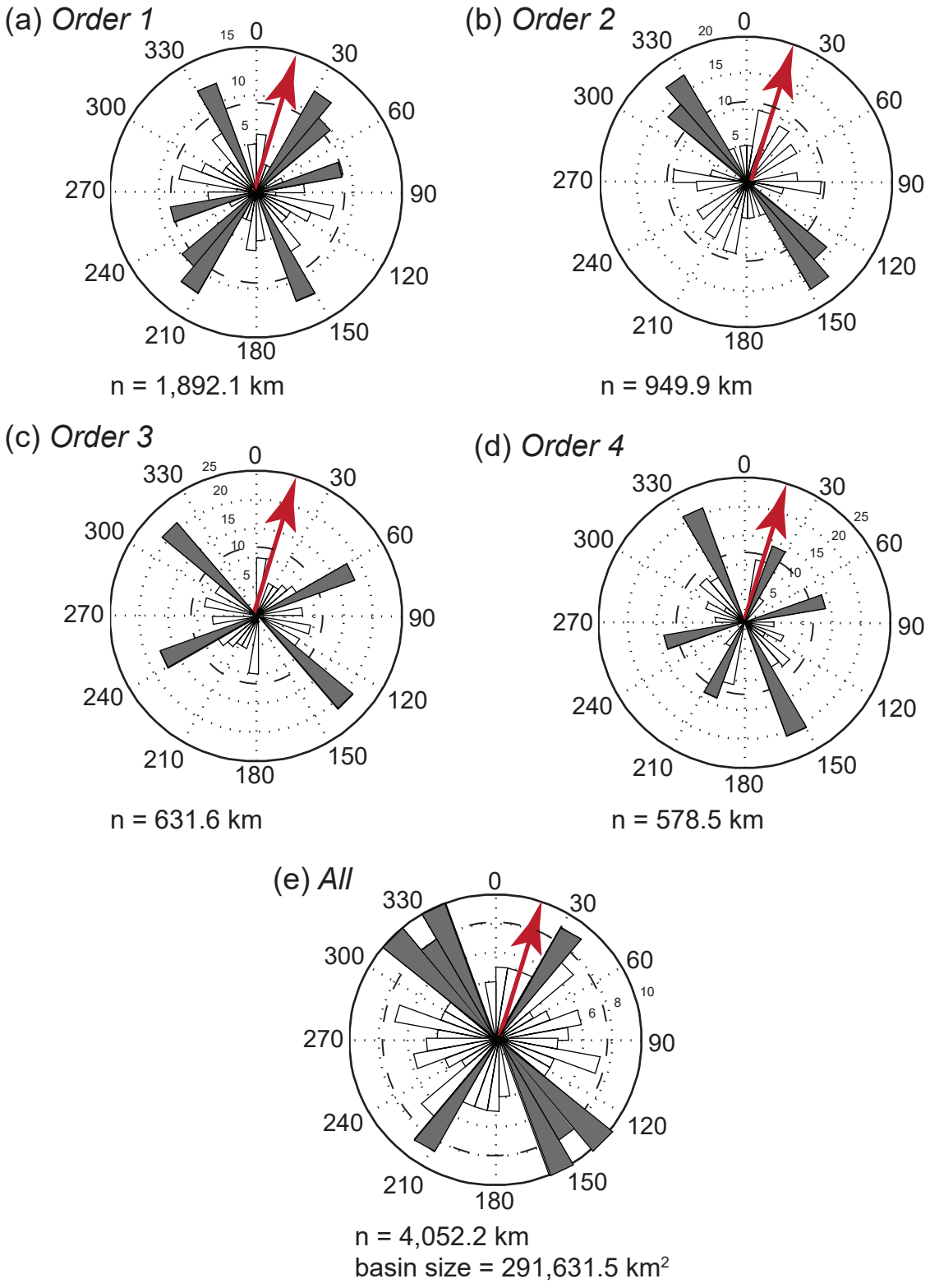

Figure F7: Rose diagrams for basin 7 for all valley segments and Strahler order 1, 2, 3 and 4.

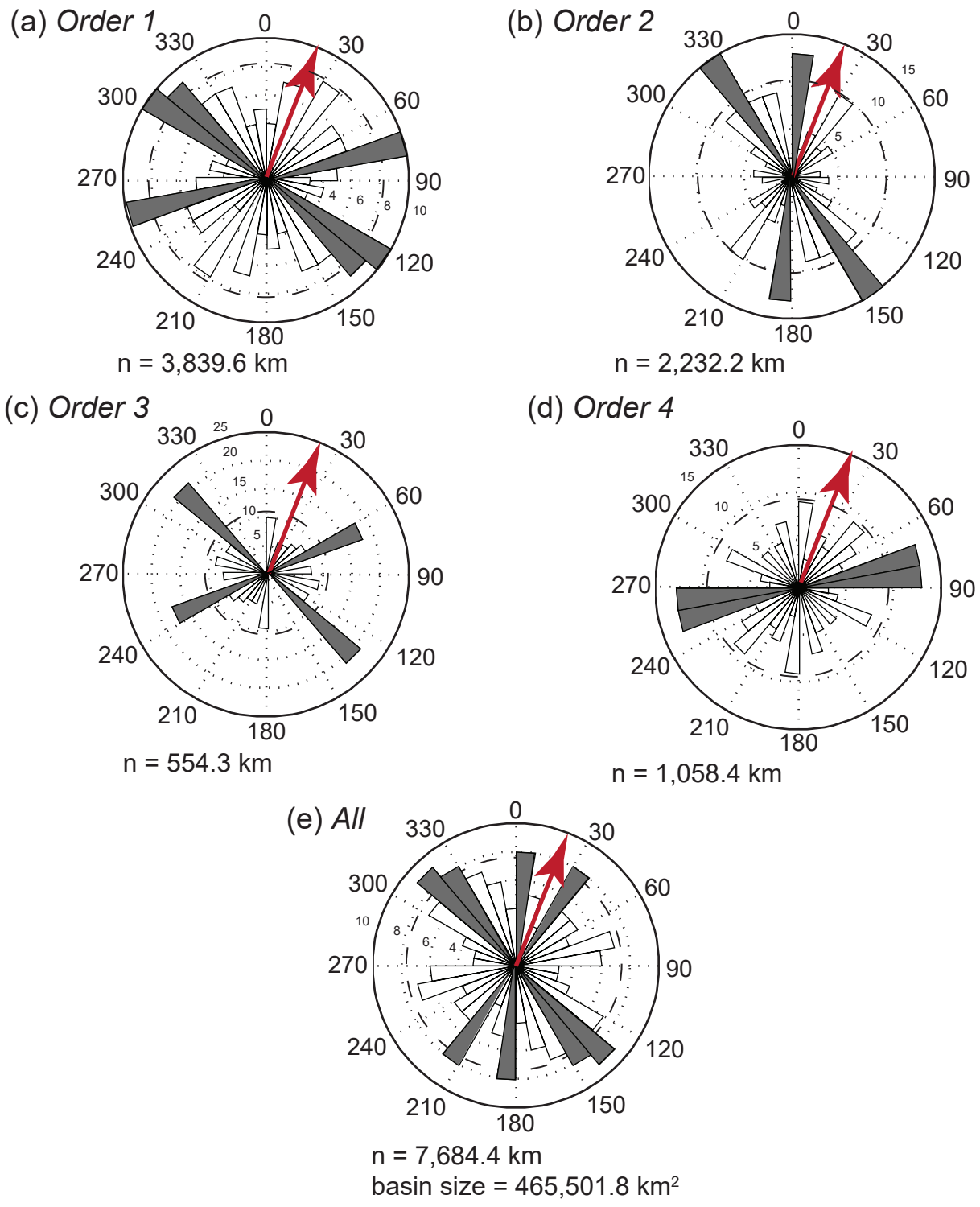

Figure F8: Rose diagrams for basin 8 for all valley segments and Strahler order 1, 2, 3 and 4.

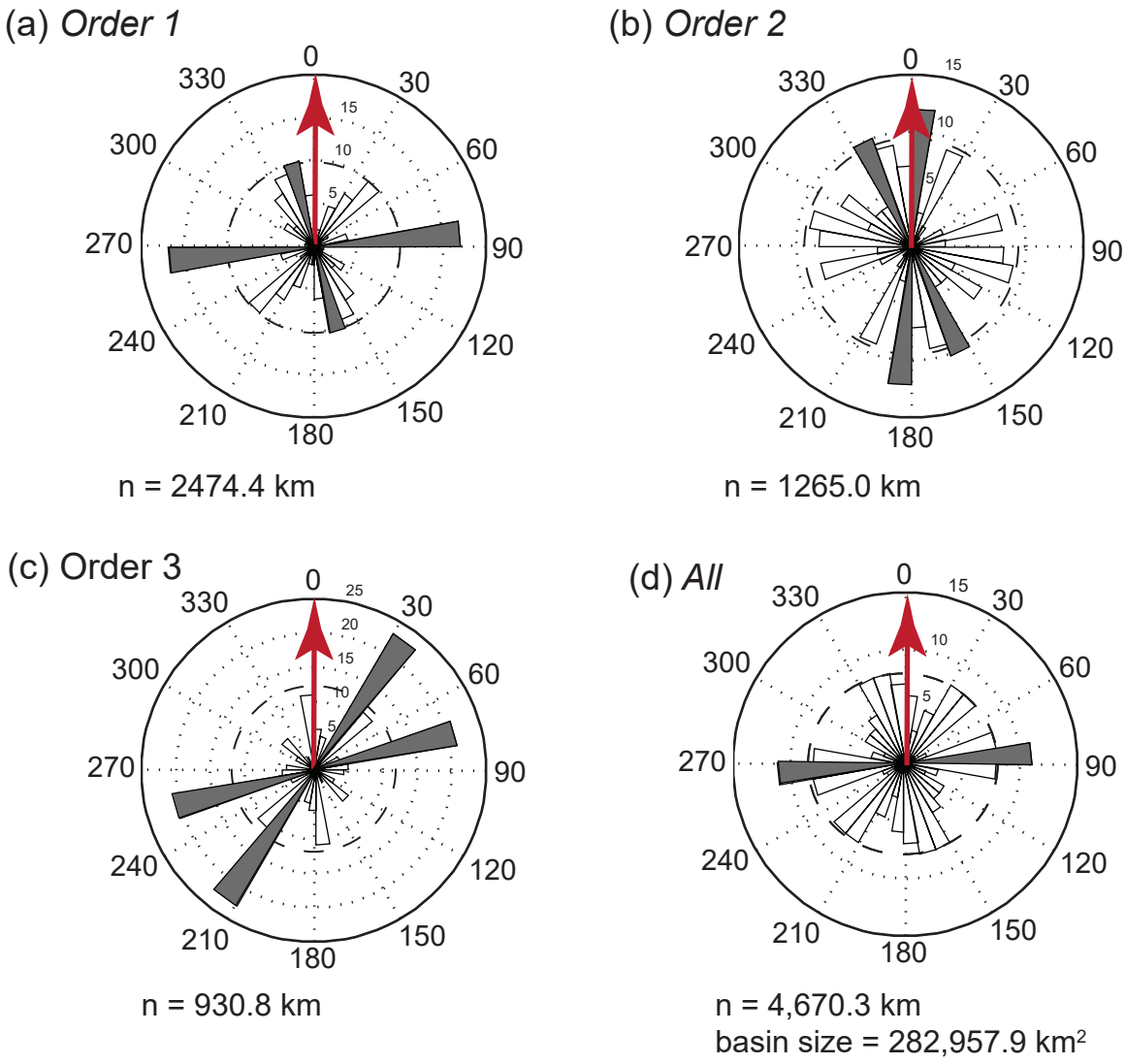

Figure F9: Rose diagrams for basin 9 for all valley segments and Strahler order 1, 2 and 3.

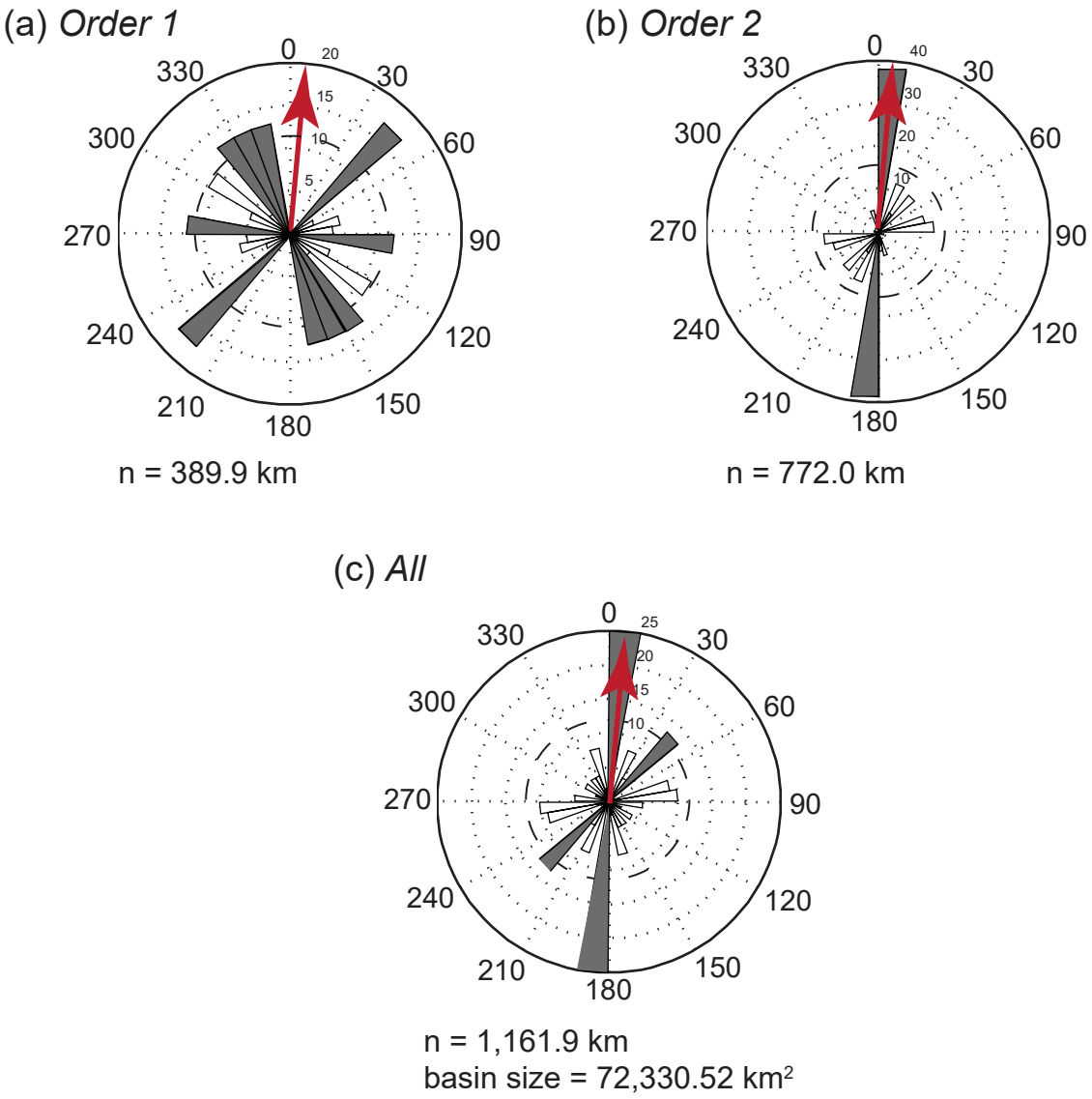

Figure F10: Rose diagrams for basin 1 for all valley segments and Strahler order 1 and 2.

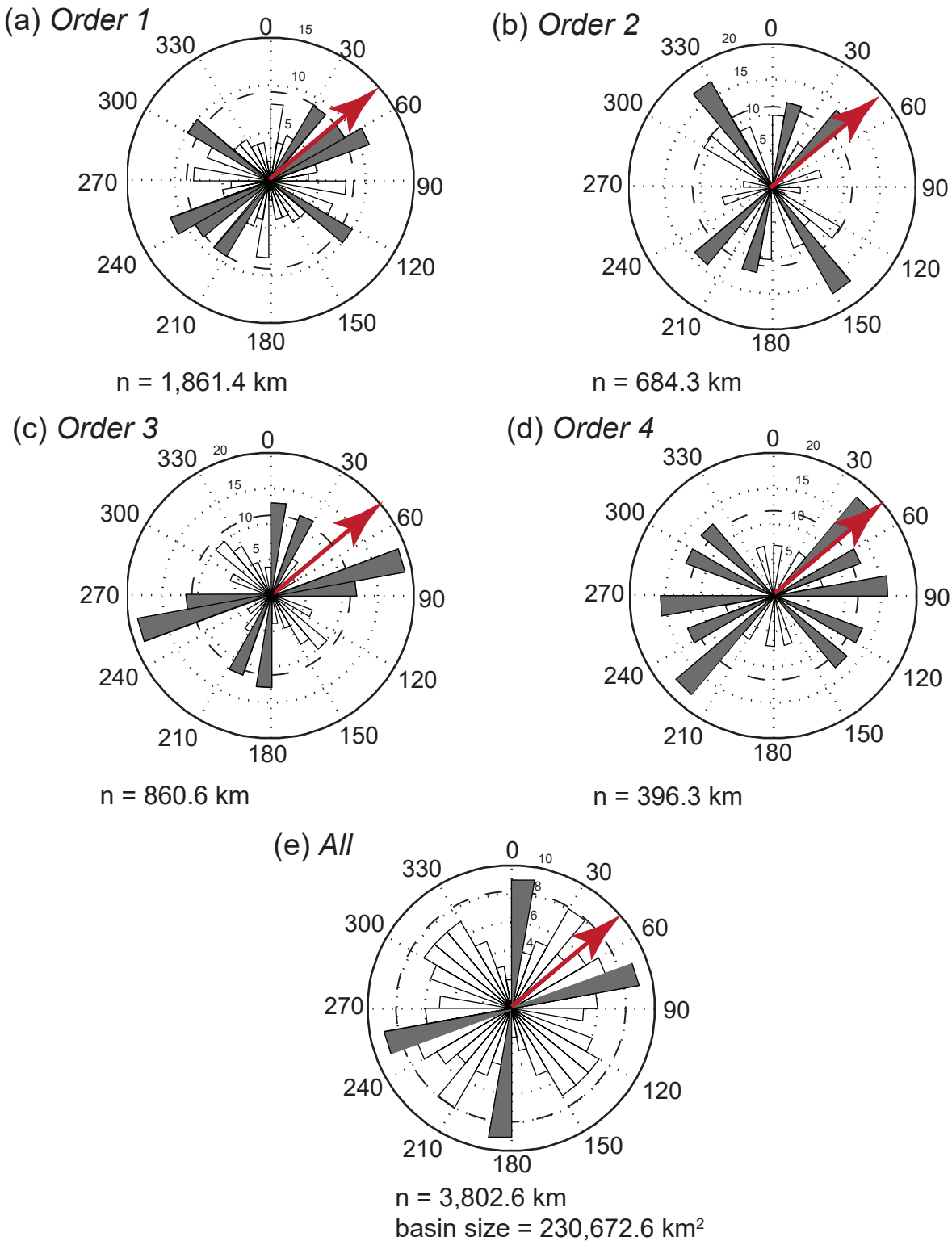

Figure F11: Rose diagrams for basin 11 for all valley segments and Strahler order 1, 2, 3 and 4.

Vita

Kelsey Anne Mason was born in Muncy, Pennsylvania where she grew up. In 2011, Kelsey graduated from Hughesville High School with Honors and was accepted to Kutztown University of Pennsylvania for a degree in Communication Design. She then switched her degree to Environmental Science in Geology and was awarded the National Science Foundation (NSF) Kutztown University Science, Technology, Engineering and Math (KU-STEM) full-tuition scholarship for academic achievement. Finally, she switched to a degree in Geology and graduated in May of 2015 Summa Cum Laude with a 3.88 GPA. During Kelsey's time as an undergraduate student, she was president of the university's Geology club, and completed undergraduate research, which she presented at the international Geological Society of America (GSA) conference in fall 2013. In the fall of 2015, Kelsey began her graduate program at the University of Texas at El Paso. During the summer of 2016, she held an internship with NASA Goddard Space Flight Center in Greenbelt, MD studying the valley systems throughout the fretted terrain on Mars and their implications for its origin. The work from this internship turned into her Master's thesis project. Kelsey held four teaching assistant positions and maintained a 4.0 GPA throughout her time as a graduate student. Kelsey is currently finishing a temporary contract with the United States Geological Survey (USGS) National Unmanned Aerial Systems Project Office (NUPO) based out of Lakewood, CO. Her job entails flying small unmanned aerial systems (sUAS), generating 3D models with structure from motion (SfM) photogrammetry software, and calibrating multispectral and thermal sUAS imagery. Kelsey hopes to continue participating in cutting-edge, meaningful and far-reaching research and is planning to obtain a longer-term position with the USGS NUPO and apply for a PhD program focusing in remote sensing.

Contact Information: kmaso270@gmail.com

This thesis was typed by Kelsey Anne Mason.